

Article

Not peer-reviewed version

---

# Brittle Fracture of Iron and Steel and the Sharp Upper Yield Point are Caused by Cementite Grain Boundary Walls

---

[Thomas Lafe Altshuler](#) \*

Posted Date: 1 July 2024

doi: 10.20944/preprints202407.0072.v1

Keywords: Boundary; Fracture; Grain; Iron; Temperature; Steel; Walls; Yielding



Preprints.org is a free multidiscipline platform providing preprint service that is dedicated to making early versions of research outputs permanently available and citable. Preprints posted at Preprints.org appear in Web of Science, Crossref, Google Scholar, Scilit, Europe PMC.

Copyright: This is an open access article distributed under the Creative Commons Attribution License which permits unrestricted use, distribution, and reproduction in any medium, provided the original work is properly cited.

Article

# Brittle Fracture of Iron and Steel and the Sharp Upper Yield Point Are Caused by Cementite Grain Boundary Walls

Thomas L. Altshuler

D.Phil. (Oxford), PE., FASM, 819 Freedom Plaza Circle, Sun City Center, FL 33573, Independent Researcher, Former owner of the Advanced Materials Laboratory, Inc., Former Visiting Professor Northeastern University, Boston, MA, thomasaltshuler@gmail.com

**Abstract:** Brittle fracture of iron and steel above twinning temperatures are caused by cementite grain boundary wall cracks. These were revealed by an Atomic Force Microscope. At temperatures below the Ductile-Brittle Transition, cracks must propagate longitudinally within the cementite walls until the stress is sufficient high for the cracks to propagate across ferrite grains. Calculations using these concepts correctly predict the stress and temperature at the Ductile-Brittle Transition required for fracture to occur. At temperatures above the Ductile-Brittle Transition for hypoeutectoid ferritic steels, dislocations must fracture these walls transversely for plastic deformation to continue. This is responsible for the upper yield point at the elastic limit in these steels followed by a large drop in stress to the lower yield point. Here the walls surround completely all of the grains. Where the walls are segmented such as in iron, dislocations can pass around the walls resulting in a gradual change from elastic to plastic deformation. The Cottrell atmosphere theory of yielding is not supported experimentally. It was the best available until later experiments including those using the Atomic Force Microscope were obtained. Methods are presented here giving yield strength versus temperature and also the parameters for the Hall-Petch and Griffith equations.

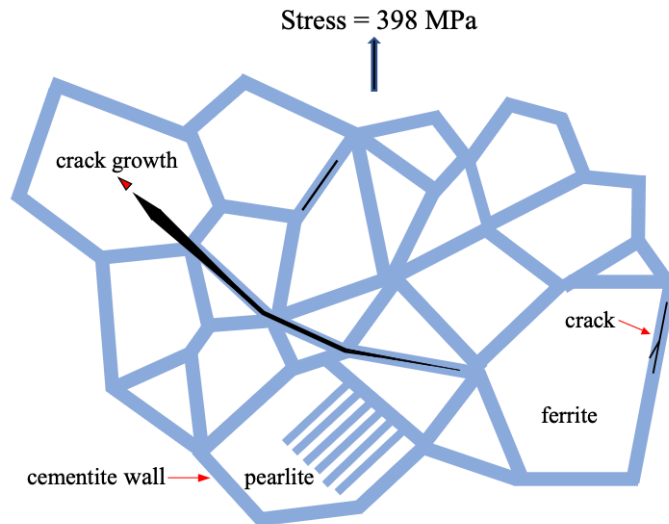
**Keywords:** boundary; fracture; grain; iron; temperature; steel; walls; yielding

---

## Fracture

### Graphical abstract

### STEEL grains – high carbon



AISI 1018 steel  
1,900 ppm carbon

DBTT =  $T_C = 5^{\circ} \text{C}$

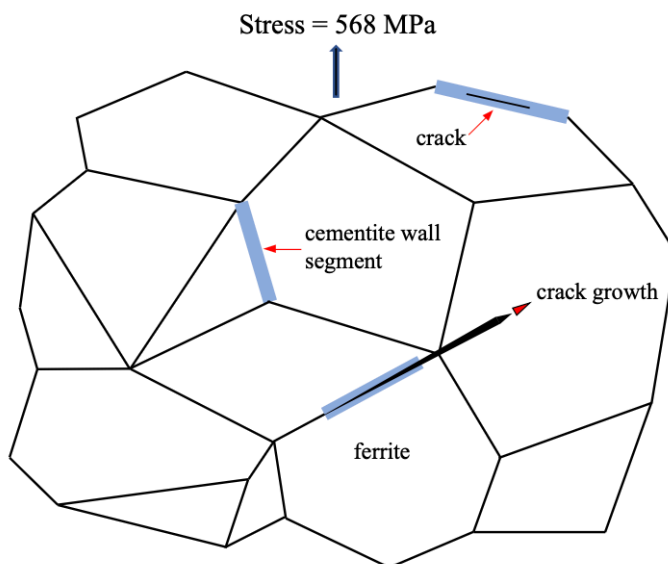
Cementite grain boundary walls surround all the grains. A crack grows first within a wall, then through adjoining walls, and then across a grain.

---

**Stress sufficient to propagate a crack in ferrite is 5 times that required for crack growth through cementite**

---

### IRON grains – low carbon



Polycrystal Iron  
10ppm carbon

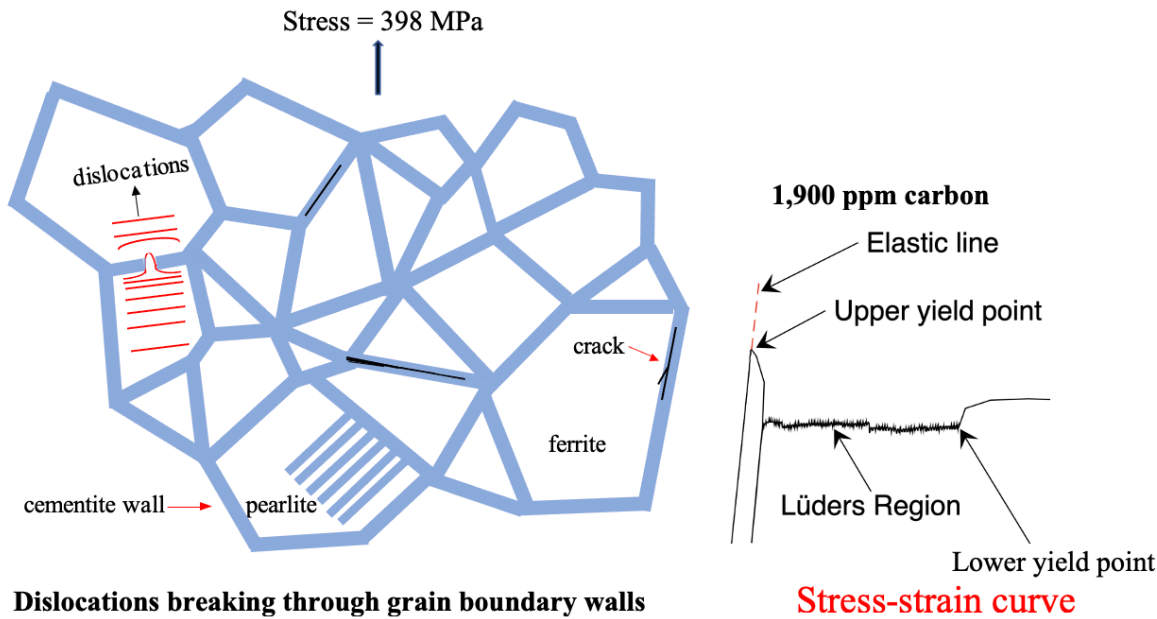
DBTT =  $T_C = -172^{\circ} \text{C} = 101^{\circ} \text{K}$

Cementite grain boundary segments do not surround all of the grain boundaries. A crack within a segment grows first in that segment to its end and then propagates into the ferrite grain.

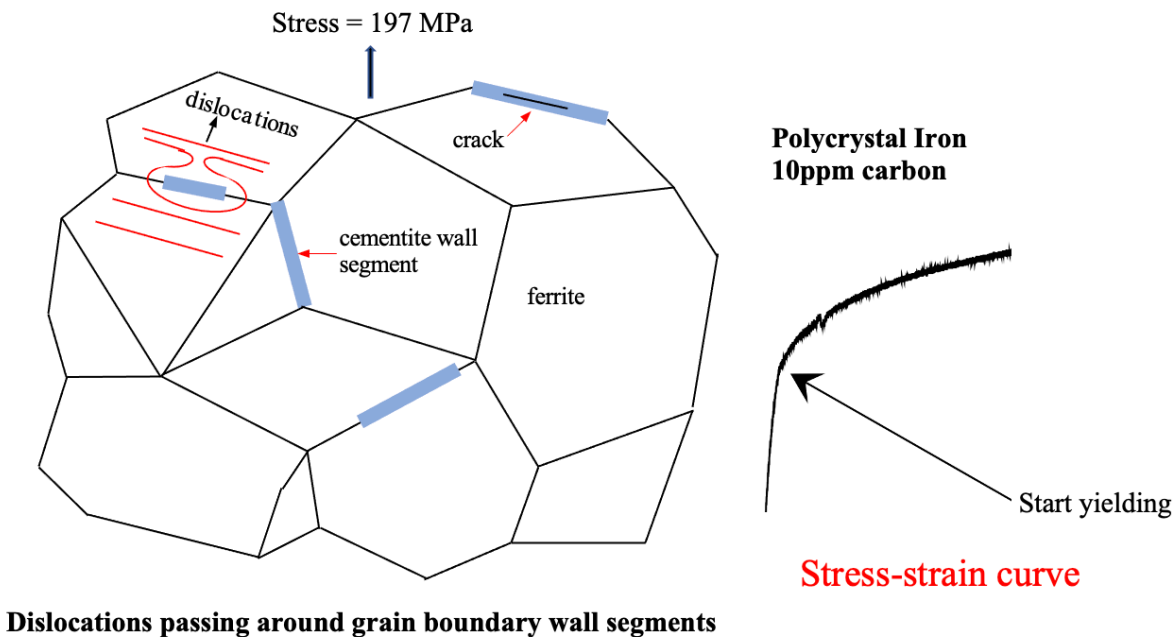
## Yielding

Graphical abstract

**STEEL grains – high carbon**



**IRON grains – low carbon**



## 1. Introduction

The unique properties of steel are caused by cementite grain boundary walls.

Steel has unique properties not found in other metals. Steel has a sharp upper yield point at the end of the elastic limit followed by a rapid drop in stress to the lower yield point. Steel has a transition from ductile deformation to brittle fracture. This occurs at approximately -5° Celsius, the Ductile to Brittle Transition Temperature (DBTT). The DBTT was responsible for Victory ships breaking in half in the north Atlantic ocean when the temperature dropped below freezing during WWII. Petch [31] found a correlation between yielding and grain size of steel. He therefore created the Hall-Petch equation. Cottrell [29] explained that the upper yield point of steel was caused by the breaking of edge dislocations from solute carbon atoms. This explanation was reasonable since it was believed that the grain boundaries of steel consisted of disordered atoms. Since there was a large drop in stress from the upper yield point to lower yield point, it was assumed that the large stress drop could not be grain boundary dependent.

Metallography of steel consists of polishing the surface of steel, etching it with nital or other etchant, and observing the results with an optical microscope. This microscope views surfaces in two dimensions. The dark lines between the grains were assumed to be grooves that etched more rapidly than the grains. This conclusion was reached because the disordered atoms at the grain boundaries had a higher entropy than those of the grains.

With the invention of the Atomic Force Microscope (AFM) that viewed surfaces in three dimension, Altshuler [3] was surprised to find grain boundary walls in AISI 1018 steel rather than grooves. He concluded that these walls consisted of cementite. Altshuler [4] also found cracks in these walls. He concluded that these cracks were caused by stresses resulting from thermal expansion differences between adjacent grains as steel cooled from austenite to ferrite and to room temperature.

Experiments by Altshuler [5] showed that the Cottrell theory of yielding was not supported experimentally, see Figure 14. He also found that iron had gradual yielding from elastic to plastic deformation, Figure 11. Steel on the other hand had a sharp upper yield point, Figure 10. Both iron and steel were saturated with interstitial carbon atoms. He therefore arrived at the conclusion that the Cottrell atmosphere of yielding was not the cause of the sharp upper yield point of steel.

The purpose of this manuscript is to show that cementite grain boundary walls in steel and iron are responsible for the unique mechanical properties of these metals. An alternative theory of yielding of steel and iron is presented. Also, it is recognized that grain boundary cracks are responsible for the DBTT. Experimental data in Figures 13, 15, and 16 provide the parameters for the Hall-Petch equation as well as those of the Griffith [1] equation. Using these parameters as well as knowledge of the grain size of iron or steel and the characteristics of the cementite grain boundary walls, one can calculate the stress and temperature at the Ductile Brittle Transition. Such calculations are presented in this manuscript. In order to provide experimental justification for this new theory of yielding and for calculation of the DBTT, three hypotheses must be satisfied, namely:

1. *Brittle grain boundary walls present in iron and ferritic hypoeutectoid steels consist of cementite with a high degree of probability.*
2. *The sharp upper yield point at the elastic line, followed by a rapid drop in stress to the lower yield point for ferritic hypoeutectoid steels, is caused by dislocations fracturing transversely cementite grain boundary walls that surround completely each grain.*
3. *Cracks in the grain boundary walls are primarily responsible for the brittle behavior of iron and steel at temperatures below the ductile-brittle transition temperature.*

As a guide to understand the structure of this manuscript, here is a brief summary. This manuscript is divided in three major parts giving results and discussion, each to satisfy the three hypotheses. These are:

### First Part for Hypothesis 1

Results given in Sections 3.1 and 3.2 give Atomic Force Microscope scans that show cementite grain boundary walls. Discussion about the grain boundary walls is given in Section 4.1 which shows:

- how the grain boundary walls formed as steel cools from austenite to ferrite, Offerman [16] and K. Lu [17].
- pearlite platelets that form and grow from grain boundary walls, Bhadeshia [18].
- the nucleation and growth of cementite at the steel grain boundaries, Pandith [19].
- observations of cementite particles in steel grain boundaries, Takahashi [21], Bin [22], and Ogawa [23].
- How the information in these discussions support hypothesis 1.

Section 4.2 presents calculations to determine the amount of carbon required to form cementite grain boundary walls. In steel, the carbon content is sufficiently high that the cementite grain boundary walls do surround all of the grains. Iron, on the other hand, has insufficient carbon for cementite grain boundary walls to surround all of the grains. Therefore, the grain boundary walls are segmented. These calculations agree with observations in Figures 1 and 8.

Calculations show that the carbon content of steel is sufficiently high that cementite grain boundary walls surround completely all of the grains, Section 4.2. In iron, calculations show that the carbon content in iron is insufficient for the cementite grain boundary walls to surround completely all of the grains.

### **Second Part for Hypothesis 2**

For yielding of hypoeutectic steels in which brittle grain boundary walls surround completely all the grains, there is a sharp upper yield point at the elastic limit. This is followed by a sharp drop in stress to the lower yield point caused by dislocations fracturing the grain boundary walls transversely and pass from one grain to the adjoining grain. The deformation properties of steel is shown in Figure 10 where there is a sharp upper yield point. Section 5.1 discusses the stress-strain curve in Figure 10.

For yielding in iron, in which the brittle grain boundary walls are segmented, there is a gradual change from elastic to plastic deformation without a sharp upper yield point. Here dislocations can pass around the wall segments from grain to grain. This is shown in Figure 11 where there is a gradual change from elastic to plastic deformation of iron. Section 5.1 discusses the stress-strain curve in Figure 11.

The Cottrell [29] atmosphere of pinning of dislocations have very minor influence in terms of causing yield points in steel. This is proven in Figure 14 where two single crystals of iron are mechanically deformed. One crystal is saturated with interstitial carbon atoms while the other has almost no interstitial carbon atoms. Here, both crystals yield at about the same stress proving that interstitial carbon atoms are not responsible for the upper and lower yield points in steel. This can be seen by comparing Figures 10 and 14. The effect of grain boundaries is eliminated by testing single crystals.

### **Third Part for Hypothesis 3**

Cracks in the cementite grain boundary walls were observed by the AFM, Figure 7. By using the AFM in tapping mode, the probe broke cementite walls leaving the walls with sharp points, Figures 2 and 9. This shows that cementite wall cracks are present in all the walls that were examined, and probably all of the walls. Since pearlite platelets have no cracks, the AFM used in tapping mode did not exhibit sharp peaks and therefore did not crack, Figure 3. When the AFM was used in contact mode, the contact force of the probe was insufficient to cause fracture of the walls at their cracks, see Figures 6 and 7.

Fracturing of steel and iron at the Ductile Brittle Transition (DBT) is caused when the stress required for plastic deformation exceeds that required for grain boundary wall cracks to propagate. For steels that have grain boundary walls that completely surround all of the grains, fracture occurs when a crack propagates longitudinally within adjoining walls until the crack is sufficiently long to progress across ferrite grains. In iron where the grain boundary walls are segmented, a crack can grow within a wall segment at a stress lower than that required for fracture. Then the stress must rise until the crack can propagate into the ferrite adjoining grain with subsequent fracture.

Yield points versus temperature can be found in Figure 13 and the Hall Petch parameters found in Figures 15 and 16. Using these concepts in which the walls consist of cementite, calculations using the Griffith [1] equation (6) correctly predict the stress and temperature that are required for fracture to occur at the DBTT, in agreement with Chao [40] and Tanaka [34]. **Determining the Hall-Petch parameters may be useful in designing steel or iron having desirable mechanical characteristics.**

2. Materials and Methods

2.1. Specimen composition

Table 1. Composition of steel and iron, ppm.

Metal	Al	C	Cr	Co	Cu	Mn	Mo	Ni	P	S	Si
Polycrystal AISI 1018 steel	300	1900	1100		500	7300	100		60	13	1400
Polycrystal iron, 14 ppm C	1.5	14.4	2.4	6.7	0.9	0.61	0.22	1.5			69
Polycrystal iron,10 ppm C [5]	<15	10	5	5	7	<0.01	<5	20	20	7	10
Single crystal iron, 0.005 ppm C	100	0.005	100		100	10	100	400	20		60
Single crystal iron,44 ppm C [6]	100	44	100		100	10	100	400	20		60

The Polycrystalline AISI 1018 steel was provided by Peterson Steel Corp., and the Polycrystalline iron, 14 ppm C, was provided by the GoodFellow Corporation. [2]. These were austenized (heated to  $\gamma$ Fe phase) for 75 minutes at 1650°F, and furnace cooled by Connecticut Metallurgical. This heat treatment was identical to that done for AISI 1018 steel examined by Altshuler [3,4] for correlation of results. The Polycrystalline iron, 10 ppm C (FePX2) specimens were annealed one hour at 500°C in a vacuum better than  $5 \times 10^{-7}$  torr by Altshuler [5]. The Single crystal pure iron was grown from Ferrovac “E” by Dr. D.F. Stein [6,7] and subsequently purified by him using a ZrH<sub>2</sub> treatment. Preparation of the specimens are described by Altshuler [5] and Altshuler and Christian [8].

2.2. Metallographic Specimens

Preparation of the metallographic specimens of the Polycrystalline AISI 1018 steel and the Polycrystalline Pure Iron including optical microscopy and atomic force microscopy was performed at Massachusetts Materials Research [9] as designed and specified by Thomas L. Altshuler. These specimens were polished and then lightly etched with 2% nital (2% HNO<sub>3</sub> and 98% ethanol) for 4 seconds, and indented with a Knoop diamond 100-gram force HK 67.9 (ASTM E384-17). Table 2 gives the specimen characteristics.

An annealed pure iron rod (Polycrystal iron, 14 ppm C) was not mechanically deformed. It was indented with a Knoop diamond 100-gram force HK 67.9 (ASTM E384-17) which also served as a reference for micrographs. These specimens were examined with an optical microscope by Massachusetts Materials Research [9] and examined using an Atomic Force Microscope (AFM) by Dr. Donald Chernoff [10].

Preparation was done after annealing a specimen of Polycrystalline iron, 10 ppm C [5] using standard metallographic techniques.

**Table 2.** Specimen characteristics.

Metal	Grain Size	Hardness	Specimen size
Polycrystal AISI 1018 steel	15.9 μm	Knoop 158	Tensile: ¼ in. diameter ASTM E8 sub-size
Polycrystal iron, 14 ppm C [9]	127 μm	Knoop 67.9	Tensile: 1/8 in. diameter ASTM E8 sub-size
Polycrystal iron,10 ppm C [5]	28.4 μm	Vickers 78.5	Compression: 0.050-inch diameter, 0.100 height cylinder
Single crystal iron [5]		Vickers 53.8	

2.3. Mechanical Tests

Polycrystalline AISI 1018 steel and Polycrystalline pure iron

Preparation of specimens for the tensile tests, designed and specified by Thomas L. Altshuler, were done by Thomas Baxter [9]. An MTS Sintech 30G tensile testing machine frame running Admet Software Version 5.07.13 was used for mechanical testing. The extensometer used was an MTS Extensometer, Model #632.13E-20, ½” gauge length, Class B2. All tests were performed at room temperature, see Figures 10 and 11.

Polycrystal iron FePX2 and Single crystal iron FeSX1 and FeSX3 [5]

Preparation of specimens for both tensile and compression tests were prepared by Altshuler [5]. The mechanical tests were performed in a cryogenic testing apparatus described [5] and [8]. The compression tests of the cylindrical specimens were performed using a semi-automatic compression testing machine for testing up to 21 specimens at cryogenic temperatures without requiring the cryostat to return to room temperature. These tests were done at room temperature and at cryogenic temperatures, see Figures 12 through 15.

2.4. Atomic Force Microscopy

A Digital Instruments Stand Alone Atomic Force Microscope with a NanoScope controller was used in contact mode in Figures 6 and 7.

A Bruker Dimension Icon Atomic Force Microscope operated by a NanoScope V controller was use in tapping mode in Figures 1 through 5 and Figures 8 and 9.

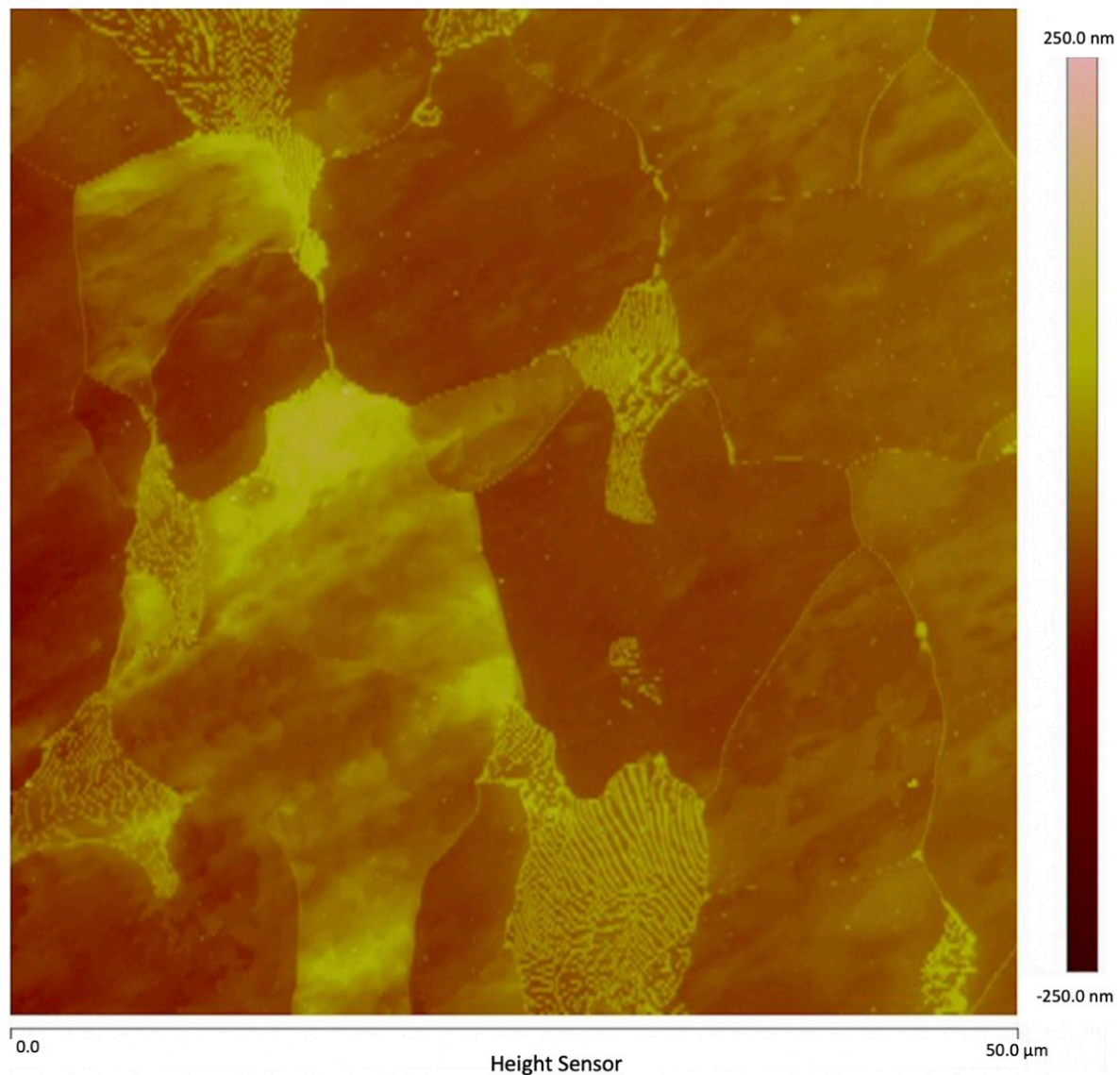
3. Results

3.1. Atomic Force Microscopy (AFM) of Polycrystal AISI 1018 steel

*These examinations were performed on specimens that were not mechanically deformed.*

A Bruker Dimension Icon Atomic Force Microscope operated by a NanoScope V controller was used for Atomic Force Microscope (AFM) examination in tapping mode, Figures 1 through 5 and Figures 8 and 9, by Dr. Donald Chernoff. The surface of the Polycrystal AISI 1018 steel was scanned with an Atomic Force Microscope (AFM), Figures 1 through 5. This steel specimen was etched with nital (2% nitric acid, 98% propanol). The relative height of various features can be seen by their color, see rightmost bar. The lines surrounding each grain consist of grain boundary walls were done with the AFM in tapping mode, Figure 1. A scan of a similar AISI 1018 steel with AFM in contact mode is shown by Altshuler (figure 14[3]). In both cases, the grain boundary wall height is the same as that of pearlite platelets which can be seen as the many light-colored lines in a grain at the lower center of Figure 1. Nital etched each grain at a different rate depending upon the crystallographic

orientation of the grain which are seen at different heights in the micrograph. The grain boundary walls and pearlite platelets were not appreciably etched by nital.



Copyright© 2020, by Thomas L. Altshuler

**Figure 1.** AISI 1018 steel.

Figure 2 shows the center portion of Figure 1 with a cross-section between two adjoining grains, see the line encircled by a white line. The top of the wall is sharp, probably due to the AFM probe used in tapping mode that broke off part of the wall. When the AFM was in contact mode, where the walls were not fractured, the top of the walls were flat, Figure 6, similar the pearlite platelets that have no cracks, see Figure 3. Also, nital did some etching of the wall. The best estimate of the actual wall width is between the two blue lines, namely 50 nm after subtracting the probe diameter.

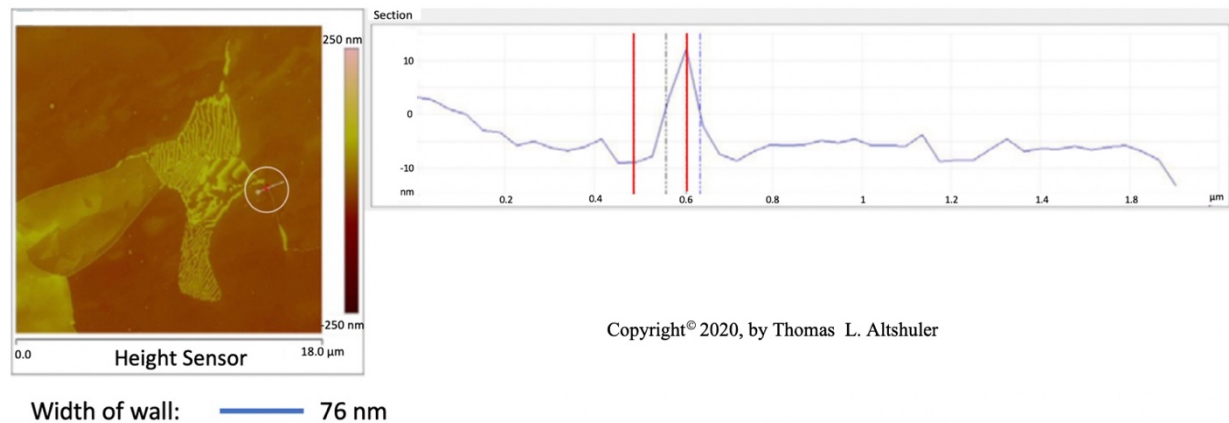


**Figure 2.** AISI 1018 steel cross-section.

The center portion of the micrograph in Figure 1 is shown in Figure 2 with AFM in tapping mode. A cross-sectional view of the grain boundary between two grains that have been etched to about the same depth is seen within the white circle. The grains were etched about 20 nm below the top of the grain boundary wall. The lines that on either side of the grain boundary wall, that establish its width, were placed half way between the top and bottom of the wall. The AFM was scanned in tapping mode. The grain boundary wall is brittle, see the crack in Figure 7. Therefore, it is believed that the probe tip fractured the wall while scanning because of a longitudinal crack in the wall, which resulted in a sharp top, Figure 2. The best estimate for wall width in Figure 2 is 56 nm by subtracting the probe tip radius of 7 nm from the measured wall thickness. The probe apex angle was  $17^\circ$ .

#### Pearlite platelets

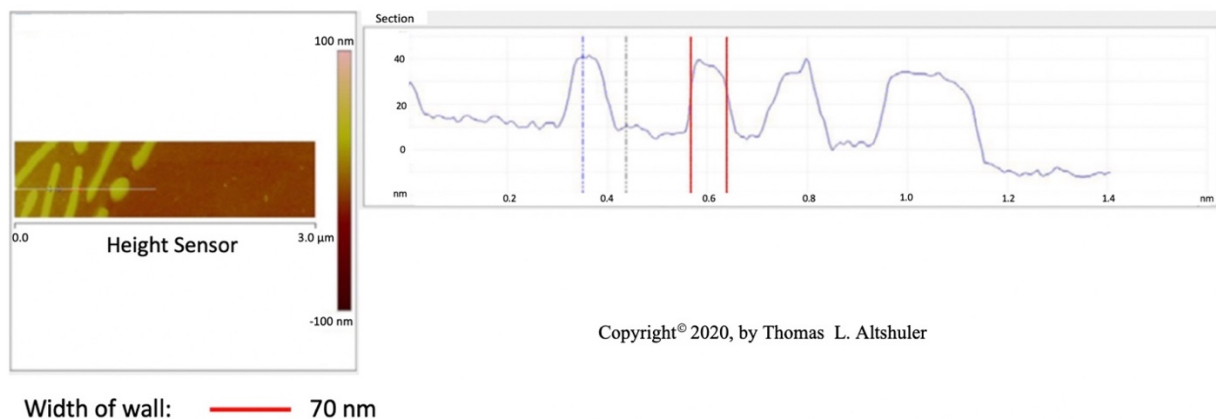


**Figure 3.** Pearlite platelets in AISI 1018 steel.

Figure 3 shows a cross-sectional view of the center portion of Figure 1. The best wall thickness is estimated to be about 59 nm by subtracting the probe diameter of 14 nm from the 73 nm in the figure. The platelets in pearlite all seem to have approximately the same width and are evenly spaced at 250 nm between platelets. Shlyakhova (Figure 2b [12]) shows that the grain boundary width is estimated to be around 70 nm. considering an AFM probe width of 30 nm. Also, he observed a pearlite platelet separation of 260 nm. Therefore, the cementite grain boundary wall thickness and the thickness of most pearlite platelets are the same with a value of  $\approx 60$  nm.

Figure 4 shows another region of the AISI 1018 steel in which the grain boundary walls can be seen surrounding each ferrite grain.

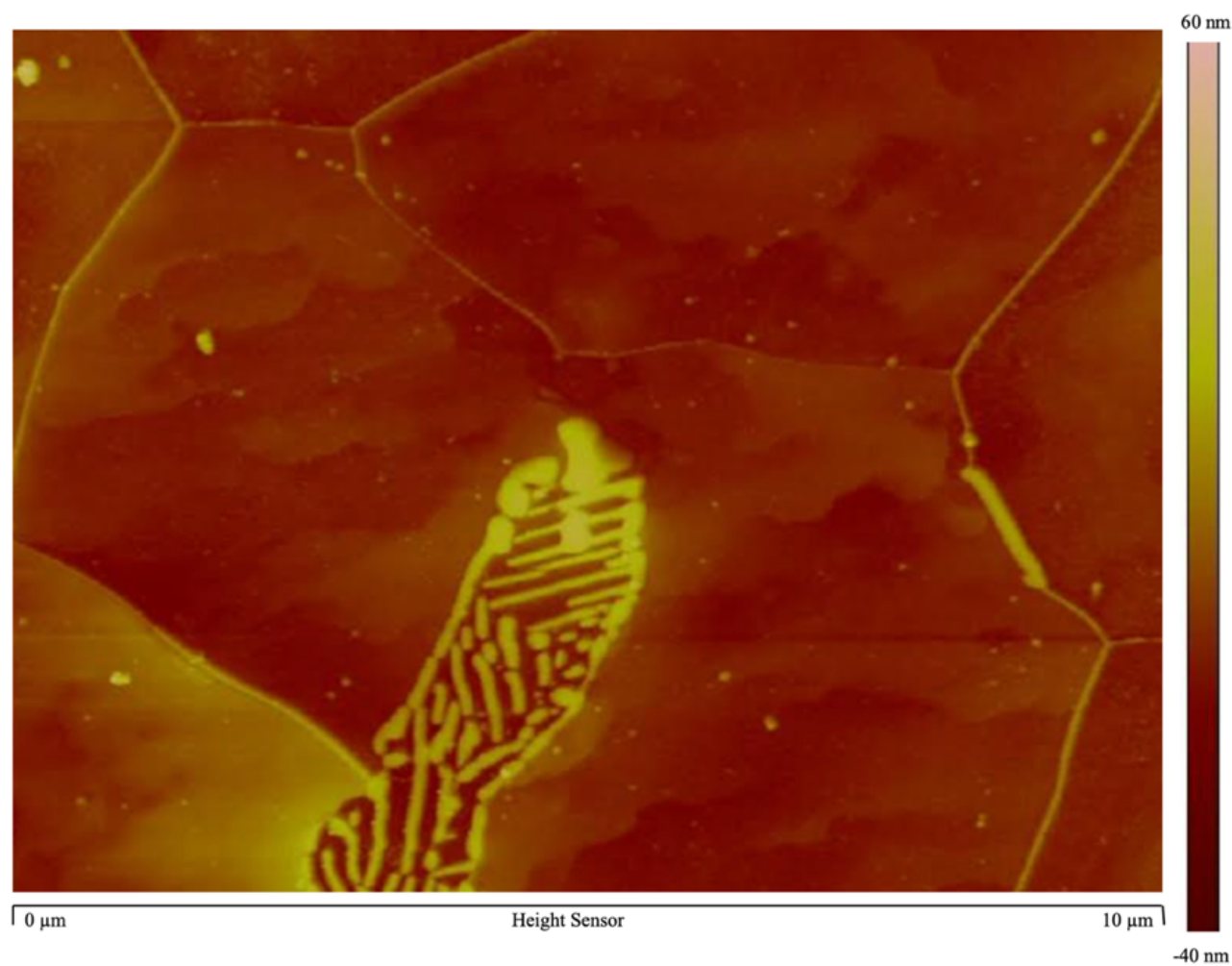
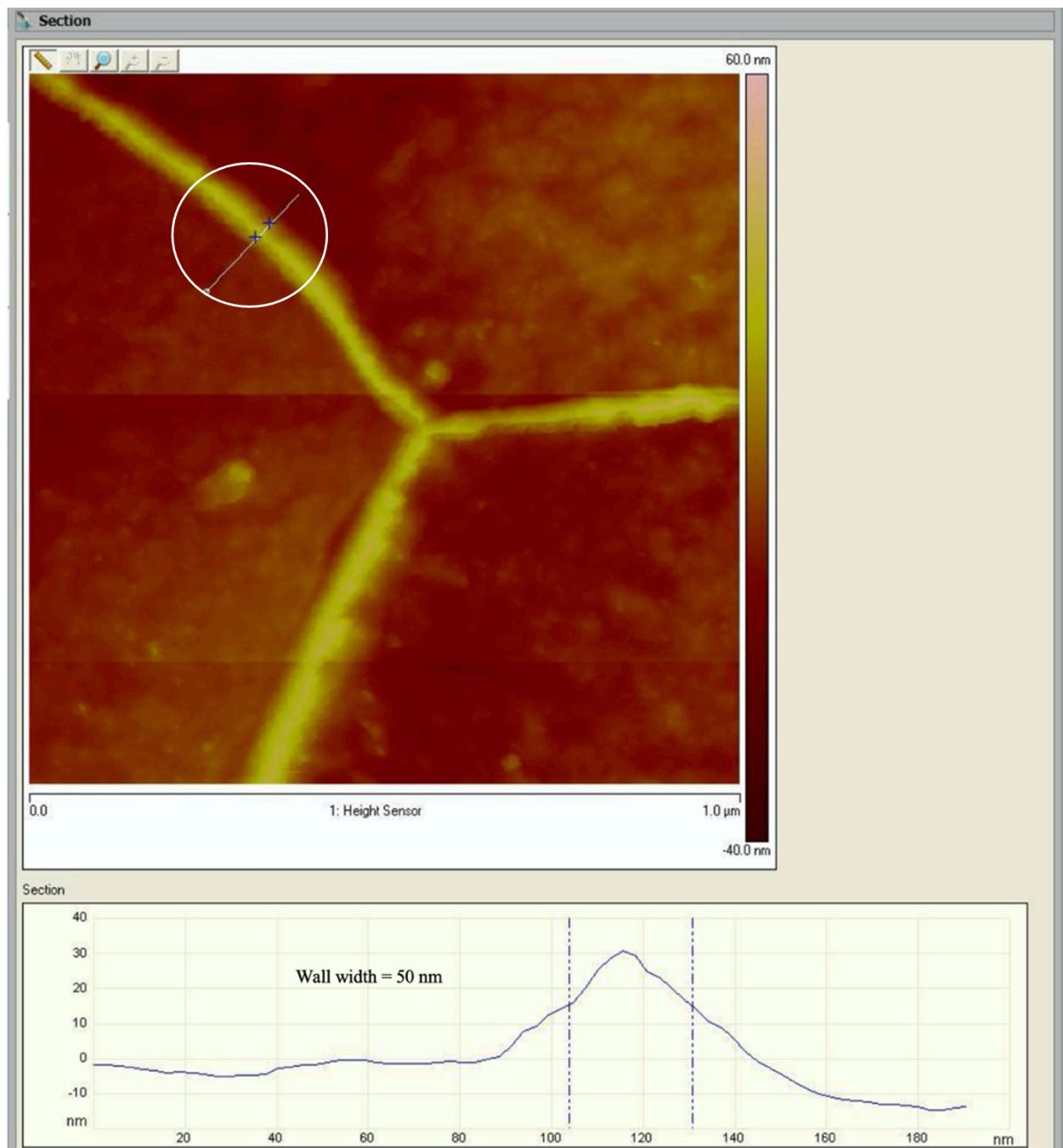


Figure 4. AISI 1018 steel.

Three grain boundary walls, AFM in tapping mode



Copyright© 2020, by Thomas L. Altshuler

**Figure 5.** AISI 1018 steel cross-section grain boundary wall.

Figure 5 shows the lower right portion of Figure 4 with a cross-section line within the white circle between two adjoining grains. The AFM is in tapping mode. The best estimate of the actual wall width is 50 nm at its base. Here the top of the walls is pointed, where the wall was fractured in tapping mode.

Three grain boundary walls, AFM in **contact mode**

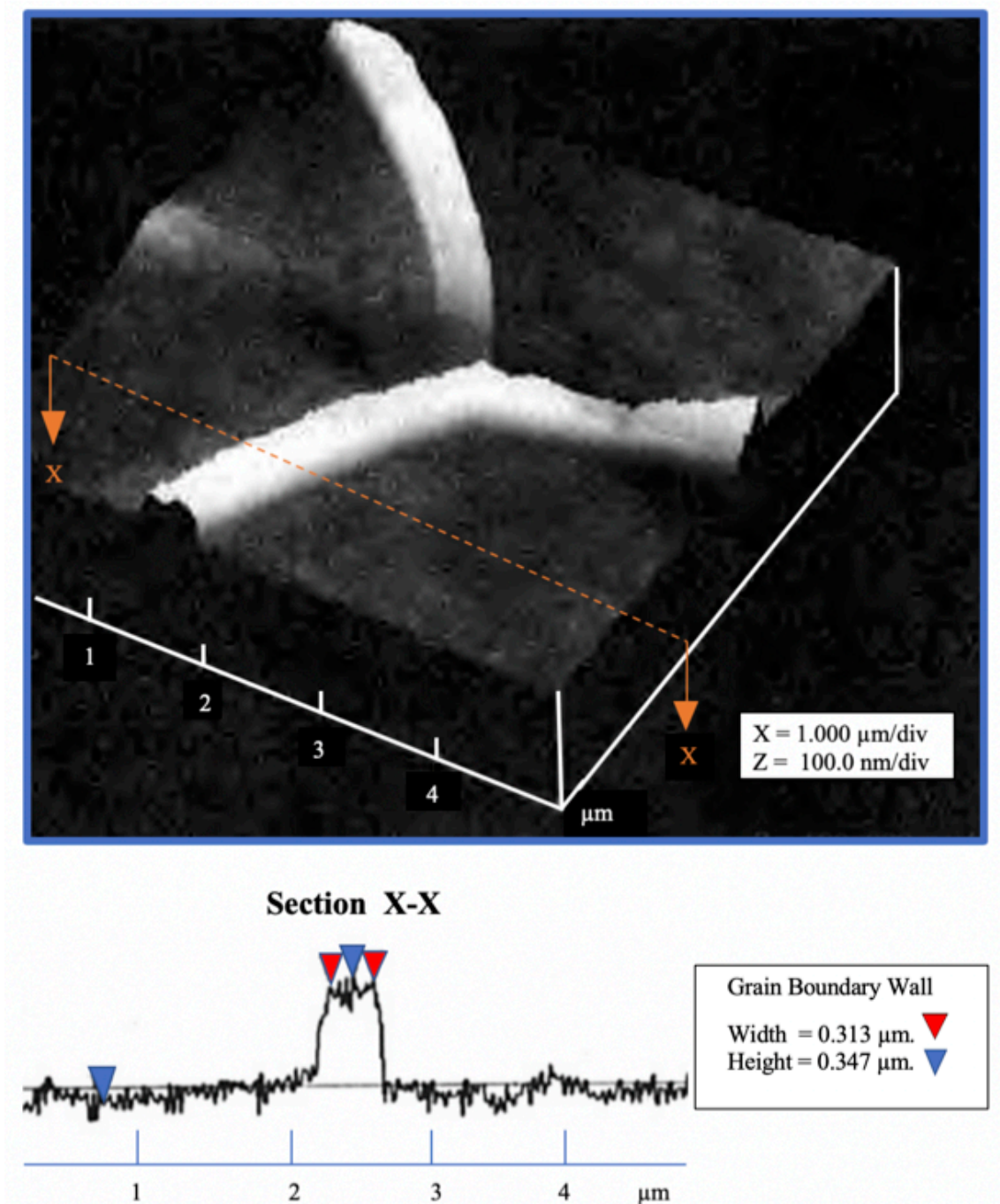


**Figure 6.** Three grain boundary walls, AFM in contact mode.

Here the top of the walls are flat, similar to the top of pearlite, Figure 3. This shows that the AFM in contact mode does not crack the walls .

Cracks in grain boundary walls

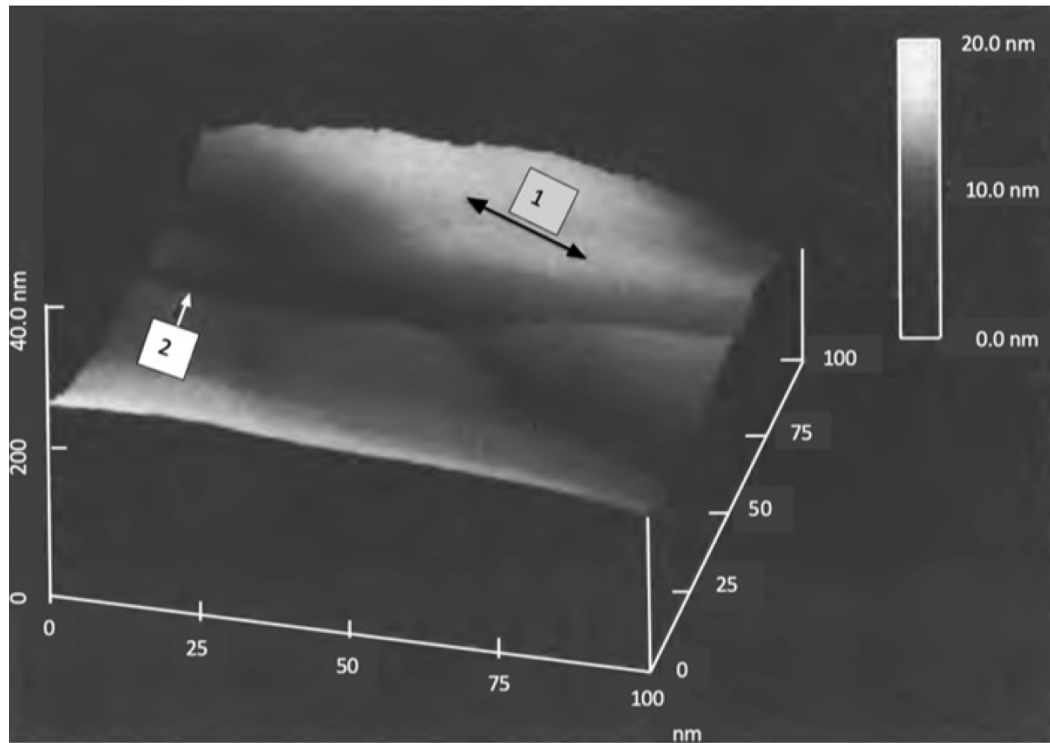


**Figure 7.** AFM of AISI 1018 steel.

The scan in Figure 7 was performed using the contact mode of the AFM probe which did not fracture the cementite wall, thereby revealing cracks. A grain boundary wall (arrow 1) shows a branched longitudinal crack (arrow 2). This indicates that the wall is brittle. In tapping mode the AFM broke the walls at the cracks, Figures 2, 5, and 9.

### 3.2. Atomic Force Microscopy of Polycrystal Iron, 14 ppm C

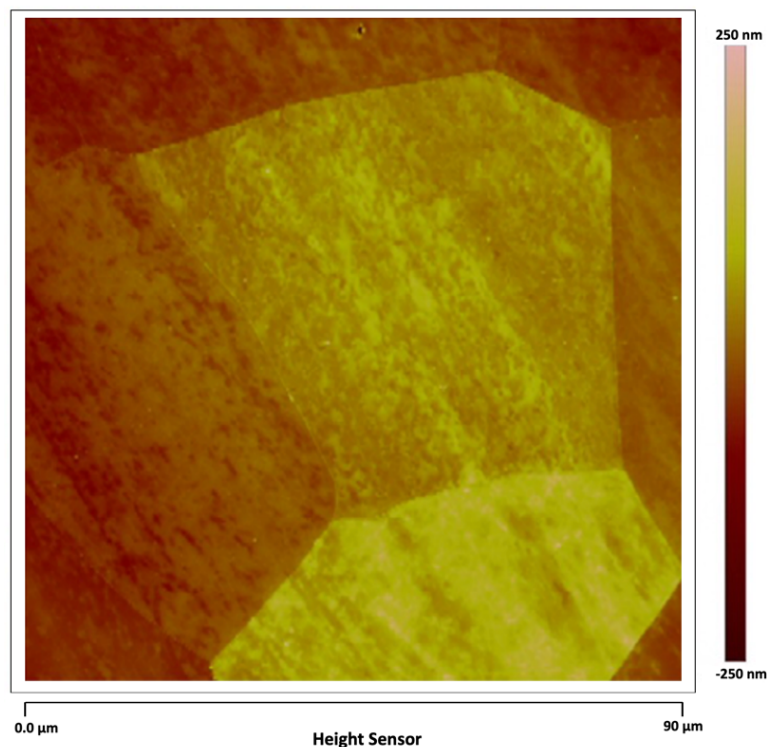


**Figure 8.** Polycrystalline iron, 14 ppm C, reprinted with permission [11].

Polycrystalline iron, 14 ppm C, was examined by an AFM, Figure 8. A grain boundary wall is visible between the center grain and the left one. No grain boundary wall can be seen between the center grain and the right grain.

The grain boundary wall between the top two grains in Figure 8 is shown in Figure 9, see the line enclosed within the white circle. The wall thickness is estimated to be 103 nm after subtracting the probe radius on both sides of the wall. The AFM was in tapping mode.

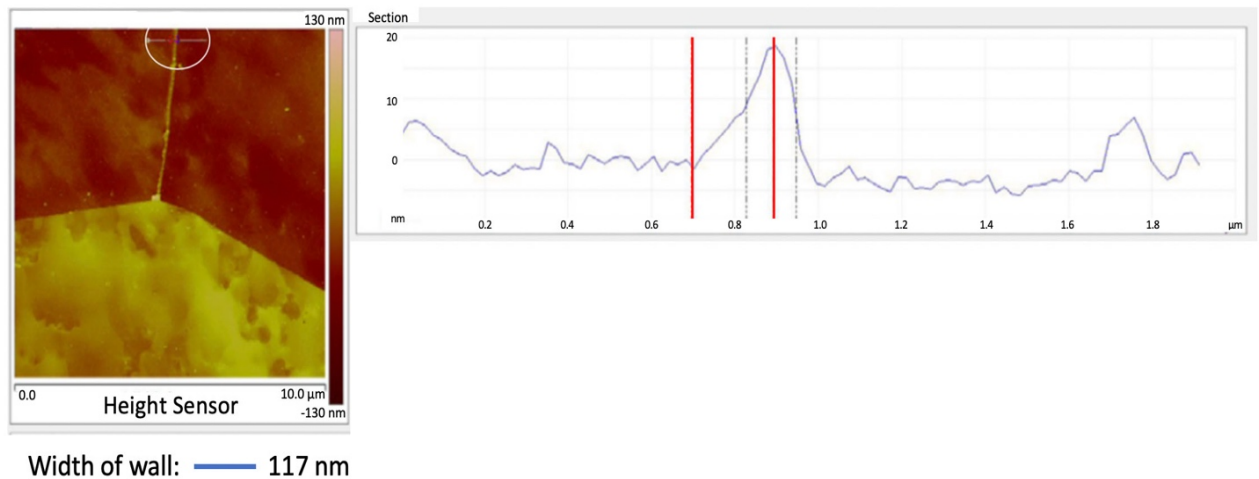


**Figure 9.** Specimen #3: Section scan across grain boundary pure iron.

### 3.3. Tensile Tests of Polycrystal AISI 1018 Steel

All tests were performed at room temperature at a strain rate of  $1.61 \times 10^{-4}$  in/in-sec. Two 0.250 diameter ASTM E8 sub-size tensile specimens were machined from annealed AISI 1018 steel rods. Three specimens were tensile tested, labelled as Specimen A, B, and E. The Rockwell hardness of specimen A was HRBW-69 and average Knoop microhardness was HK 158 with a 100-gram load. A 0.125 diameter ASTM E8 sub-size tensile specimen was machined from a rod of Polycrystal iron, 10 ppm C. It was tensile tested and labelled as Specimen C. The Rockwell hardness was HRBW-14.5 and average Knoop microhardness HK 67.9 with a 100-gram load.

The annealed AISI 1018 steel, Specimen A, was tested to failure. Figure 10 shows the stress-strain curve until the extensometer was removed. Testing was then continued. The ultimate tensile strength was 486 MPa. and total elongation was 38%. Stress and strain values that follow are taken from the data tables generated by the computer of the tensile testing machine.

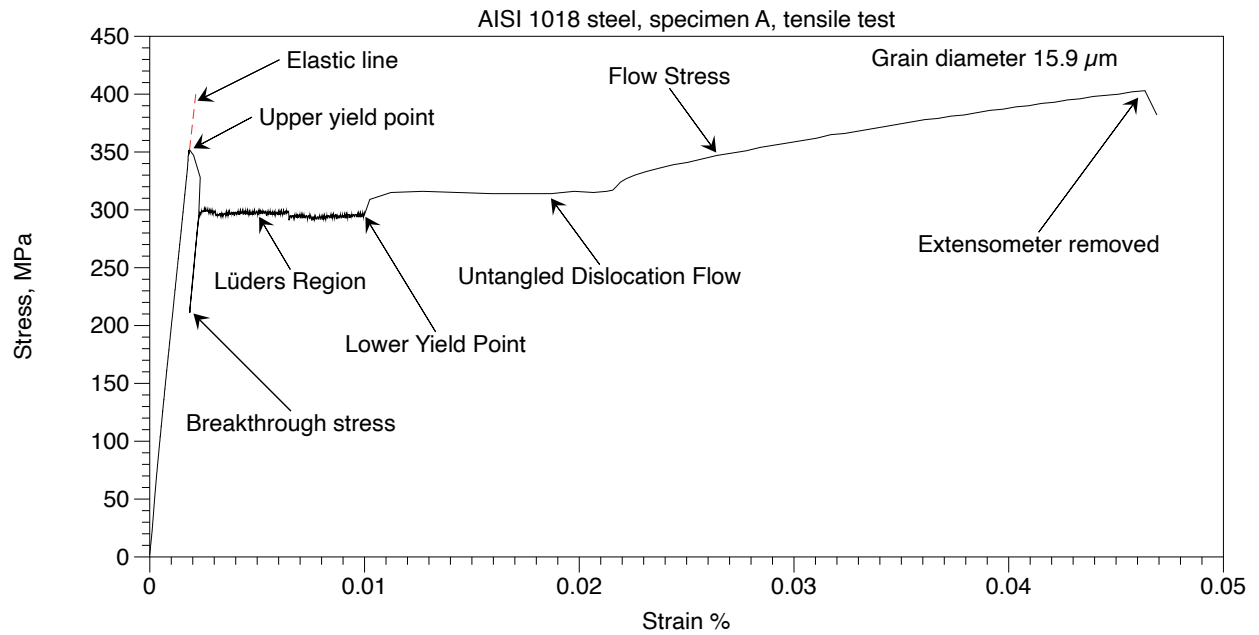


**Figure 10.** AISI 1018 steel, Specimen A, tensile test.

### 3.4. Tensile Tests of Polycrystal Iron, 14 ppm C

Two tensile tests were performed on Polycrystal Iron, 14ppm C. These were done in the same way that was done with the Polycrystal AISI 1018 steel. In Figure 11, deformation continued until the specimen broke at a strain of 0.0698. A similar specimen, Specimen D, broke in the grips in the Ripple Stress Region. Prior to failure, the stress-strain curve was like Specimen C.

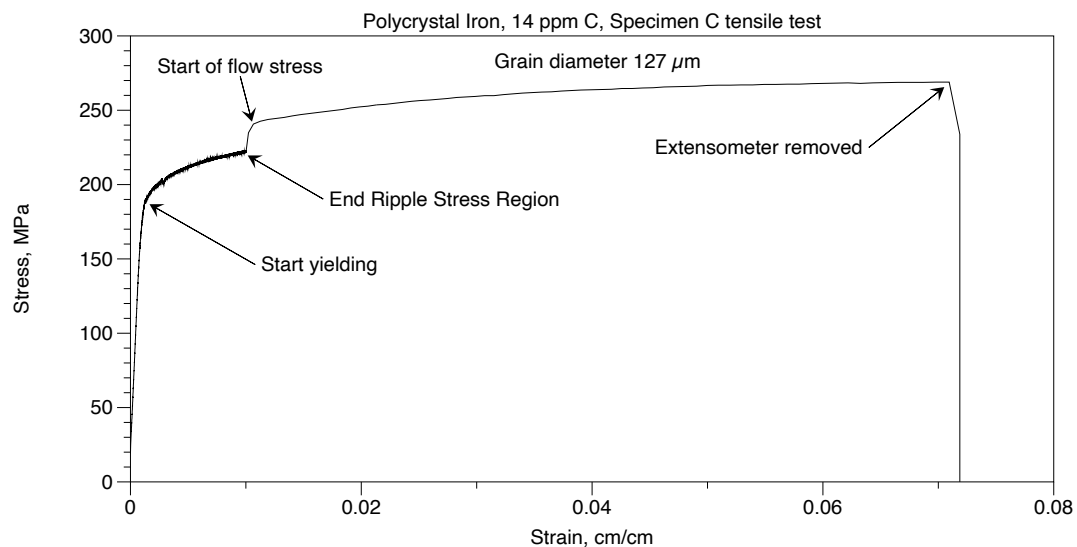


**Figure 11.** Polycrystal iron, 14 ppm C, tensile test.

## 4. Discussion about grain boundary walls

### 4.1. Cementite grain boundary walls

In steel, cementite ( $\text{Fe}_3\text{C}$ ) appears to be formed at the grain boundaries of AISI 1018 steel as shown with AFM scans, Figures 1, through 9. This hypothesis was proposed by Altshuler [3,4] as a result of the first Atomic Force Microscope examination of steel. This concept can be supported from the following arguments. If the grain boundaries consisted only of disordered atoms of pure iron, due to their higher entropy compared to that of the ordered atoms in the crystal lattice within

the ferrite grain, the boundaries should etch at a more rapid rate than the grains themselves. Thus, the grain boundaries should be depressed compared to the adjacent grains which is generally believed to be true. However, the grain boundaries form walls which are at a height equally to that of the pearlite platelets above the ferrite portion of the grains as measured by the AFM scans. This means that the walls must consist of stable molecules, and etch at the same low rate as that of the cementite platelets. These walls must also consist of carbide since the amount of carbon in the steel is by far the most abundant element present that could form an ionic crystal with iron, see Table 1. The surface of the steel was observed with an optical microscope using differential interference contrast, suggested by Wells [13]. Both the pearlite platelets that consist of cementite and the grain boundary walls rotate polarized light by the same amount. This indicates that they probably consist of the same intermetallic compound. Cementite is a brittle intermetallic compound. The walls also are brittle due to the cracks within the walls, Figure 2. McMahon and Cohen [14] observed cracks in carbide particles in the grain boundaries of iron.

#### Published observations of cementite in grain boundaries

*The following observations show that cementite exists in the grain boundaries. Also, it is shown how grain boundary walls of cementite could form so that they surround completely each grain, and that cementite may be the dominant factor of yield strength.*

The following discussion shows why the grain boundary walls surround completely each grain in hypoeutectoid steels. This is due to the formation of these walls as steel cools from 900°C to room temperature, which occurs in the following sequence:

- 900°C steel grains are austenite.
- 822°C ferrite nuclei begin to form with subsequent growth of grains.
- 727°C is the eutectoid temperature. The solute carbon is 0.0218 wt. %.
- 716°C the solute carbon is 0.019 wt. % in AISI 1018 steel. Ferrite grains are fully formed.
- ~ 715°C solute carbon is below 0.019 wt. % and the excess carbon atoms diffuse to the grain boundaries and combine with iron atoms forming Fe<sub>3</sub>C (cementite).
- 639°C grain boundary walls are fully formed based on 781 ppm carbon for AISI 1018 steel, see section 4.2. Then pearlite platelets begin to grow from the grain boundaries.
- ~ 400°C the pearlite platelets have essentially completed their growth.
- 20°C ferrite grains have less than 0.5 ppm carbon in solid solution, Hume-Rothery [15].

#### Sequence of grain boundary walls and pearlite formation versus temperature

Published work by various authors substantiate this sequence of grain boundary wall formation and pearlite platelet formation. Offerman [16] showed, with a monochromatic beam of hard x-rays, that when steel, up to 2 wt. % carbon is cooled from austenite at 900°C to 600°C in one hour, ferrite nuclei form rapidly at 822°C. New nuclei of ferrite continued to form until pearlite started to transform at 685°C. Therefore, grains of ferrite were already formed prior to formation of cementite. This shows why cementite walls grow and surround completely each grain. Pearlite then grows from whatever solute carbon atoms remain within the ferrite grains due to diffusion of carbon atoms along grain boundaries, according to K. Lu [17].

#### Formation and growth of pearlite platelets at the grain boundaries

Bhadeshia, (figure 18 [18]), describes the process for formation of pearlite platelets that grow from the grain boundaries. He states that pearlite evolves with the nucleation of ferrite at the austenite - ferrite grain boundary wall. It appears, from his TEM micrograph, that the pearlite platelets are attached to a wall. Since this can be seen in Figures 1 and 3, it seems reasonable that grain boundaries consist of cementite walls that create nucleating sites for the formation and growth of pearlite platelets. Based upon the experimental results of Figures 1, 3, and 4, it appears that cementite usually grows in width up to about 60 nm and then stops getting wider. This is possibly due to thermodynamic reasons in which the Gibbs free energy is insufficient for the continued growth in width of the cementite grain boundary wall. However, the lengthwise growth of the pearlite

platelets continues until all the interstitial carbon in the ferritic hypoeutectoid steel is converted into cementite as the steel cools from austenite.

#### Nucleation and growth of cementite at grain boundaries

Pandith [19], describes the nucleation and growth of cementite at high Gibbs free energy sites thus lowering that energy. Song [20] examined ultrafine ferrite grains in plain carbon Fe-Mn steel (3.1% C). The ultrafine grains (0.9-2.2  $\mu\text{m}$ ) and subgrains (0.6 - 1.5  $\mu\text{m}$ ) had particles of cementite at the junctions between three adjoining grains where the Gibbs free energy is highest. These particles are shown in white at the junction between grains, (figure 2, page 6 [20]). He also noted some fine white lines at grain boundaries where the angular difference in crystallographic orientation of the grains were between  $2^\circ$  and  $15^\circ$ . These presumably grew after cementite particles grew at the grain junctions. This might be caused by a lower Gibbs free energy at grain boundaries compared to that at grain boundary junctions. Based upon the fine white grain boundary lines in Figure 8, the thin white lines [20] are believed to be fine walls of cementite since they are attached and grow from the cementite particles at the junctions of three grains. The black lines, shown by Song, indicate grain crystallographic misorientation between  $15^\circ$  and  $63^\circ$ . These high angle grain boundaries occupied a large fraction of the microstructure (55-70%), and show no evidence of cementite. It appears, therefore, that the creation of cementite between two grains occurs more easily when the crystallographic misorientation angle is small compared to grains with large crystallographic misorientation angles.

#### Cementite particles in grain boundaries

Takahashi [21] made quantitative observation of grain boundary carbon segregation in 0.0034 wt.% steel. He estimated that the total carbon atoms segregated in all grain boundaries was estimated to be about 2ppm by weight. Bin [22] observed nanoscale cementite precipitates of size ~20-30 nm in hypoeutectoid steels that contribute to the yield strength. Ogawa, (figure 1(a)[23]), observed cementite particles in steel containing ferrite and pearlite. He considered that the dominant factor of yield strength was precipitate strengthening by cementite particles. Bhadeshia [18] showed that the stacked plates of cementite and ferrite, namely pearlite, forms and grows from the grain boundaries between austenite and ferrite, which agrees with Figures 1 and 3. Ganev [24] noted cementite particles in the grain boundaries (over 40%) in steel which contribute to the yield point of steels with 0.10%C and 0.45%C. This establishes that cementite is seen in the grain boundaries, which are actually grain boundary walls.

These arguments are summarized and support the following hypothesis.

- Grain boundary walls have the same height as pearlite platelets. They are etched with nital like pearlite platelets thereby establishing that they are cementite.
- The grain boundary walls must consist of a carbide intermetallic compound since carbon is by far the largest impurity in AISI 1018 steel. Calculations and measurements show that ~ 40% of this carbon is in the grain boundary walls, the rest is in pearlite, see section 4.2.
- The grain boundary walls and pearlite platelets rotate polarized light by the same amount.
- The grain boundary walls have cracks as observed by the AFM, Figure 7.
- The grain boundary walls are brittle like cementite and were fractured with the AFM probe in tapping mode. Therefore, the top of the walls are pointed showing that part of those walls were fractured off of the remaining part, see Figures 2 and 5. On the other hand, since pearlite platelets have no cracks, the top of these platelets are flat and were not fractured with the AFM probe in tapping mode. When scanning the grain boundary walls with the AFM probe in contact mode, since the scanning force is gentle, the probe does not crack the grain boundary walls. As a result, the top of those grain boundary walls were flat, see Figure 7.
- Referenced literature states that cementite has been found in the grain boundaries.

- Carbide grain boundary walls grow by diffusion of carbon atoms to grain boundaries when steel cools from the austenitic temperature of 900°C to 639°C. By that temperature, the walls have fully formed around the grains. Any excess carbon then causes pearlite platelets to grow from the grain boundaries, Bhadeshia, (figure 18 [18]). Therefore, the grain boundary walls must be the nucleating site for the pearlite platelets. As a result, both the carbide grain boundary walls and pearlite platelets must have the same crystallographic structure, that of cementite.

**The hypothesis “Brittle grain boundary walls present in iron and ferritic hypoeutectoid steels consist of cementite with a high degree of probability.” is shown to be valid.**

#### 4.2. Grain boundary walls surround completely the grains or are segmented.

It is observed in Figure 1 and by Altshuler (figure 14 [3]), grain boundary walls do completely surround all of the ferrite grains. This observation is confirmed in the discussion that follows.

Carbon content required for cementite grain boundary walls to surround all of the grains.

Assume that the grain boundary walls consist of cementite. To estimate the percent of carbon in the grain boundary walls, assume that each grain consists of a hexagonal prism whose edges are at the center of the grain boundary wall. Let (D) be the grain diameter. Let the height of the hexagonal prism equal to (D). Let the length of an edge of the hexagonal face be  $L_o$ .

$$L_o = 0.27491 D \quad (1)$$

Let the grain boundary walls of cementite have a thickness of (t). The volume of the prism would be  $(\pi D^3/4)$ . The volume of the grain boundary walls is  $(2.43486 \cdot t D^2)$ , where each wall is shared equally between adjoining grains. Therefore, the ratio of the volume of the grain boundary walls to prism volume is  $(3.10015t/D)$ . The atomic weight of carbon is 12, for iron is 55.9. The weight percent of carbon is 7.16% of the weight of iron for  $(Fe_3C)$  and 6.68% of the weight of the total wall. Let  $C_o$  be the total carbon in the steel. Then the carbon by weight within the cementite grain boundary walls that is needed to completely surround all of the grains is  $(C_{ow})$ . Here  $C_{ow} < C_o$  for this condition to exist where any excess carbon goes into pearlite.

$$C_{ow} = 0.207022 t/D \quad (2)$$

#### Polycrystal AISI 1018 Steel, 1900 ppm C.

*The cementite grain boundary walls completely surround all of the grains.*

The AISI 1018 steel grain diameter was 15.9  $\mu m$ . From Figure 2 the grain boundary wall thickness (t) = 56 nm. From equation (2), the weight percent of carbon in the grain boundaries was 781 ppm. This assumes that the grain boundaries consist of cementite which surround completely each grain. The excess carbon,  $(1,900 - 729) = 1,170$  ppm, would go into the platelets of pearlite for AISI 1018 steel with 1,900 ppm carbon, Table 1. Calculations were made showing that the percent of platelets to the pearlite area was 22.4% in Figures 1 and 2. Roughly half that amount was in the other pearlite areas in Figure 1. That resulted in 1.5% platelet area compared to the total area given in Figure 1. Since 6.68% carbon is in the grain boundary wall, the carbon content of cementite in the pearlite was calculated to be  $(0.015 \times 0.0668) = 1,002$  ppm. This roughly agrees with 1,170 ppm carbon in pearlite from Figures 1 and 2. These results demonstrate that the grain boundary walls do surround completely each grain and that the remaining carbon form the observed pearlite platelets. *Therefore, cementite grain boundary walls do indeed completely surround all the grains in hypoeutectic steels.*

#### Polycrystal pure iron, 14 ppm C.

*These cementite grain boundary walls are segmented.*

The grain boundary wall width (t) was 117 nm, Figure 9. For the grain diameter  $D = 127 \mu m$ , from equation (2) the amount of carbon required for cementite walls to completely surround all the grains would be 191 ppm. Since the amount of carbon in the iron ( $C_o$ ) = 14 ppm, then the percent of the grain boundaries that have cementite walls is  $C_o/C_{ow} = 7.3\%$ .

*These walls are segmented consistent with Figure 8.*

#### Polycrystal pure iron, 10 ppm C.

*These cementite grain boundary walls are segmented.*

Assume that the grain boundary wall width ( $t$ ) was  $0.117\ \mu\text{m}$  like that of Polycrystal 14 ppm C, examined with the AFM. For the grain diameter  $D = 28.4\ \mu\text{m}$ , from equation (2) the amount of carbon required for cementite walls to completely surround all the grains would be 853 ppm. Since the amount of carbon in the iron ( $C_0$ ) = 10 ppm, then the percent of the grain boundaries that have cementite walls is  $C_0/C_{\text{ow}} = 1.2\%$ . *These walls are segmented.*

## 5. Discussion about plastic deformation of iron and steel.

### 5.1. Stress-strain curves for AISI 1018 steel 1900 ppm carbon.\_

The stress-strain curve, Figure 10 is given to show that the unique properties of steel and that these properties are real and the result of three tests. Here are the upper and lower yield point of Polycrystal AISI 1018 steel with a grain diameter of  $15.9\ \mu\text{m}$ .

In Figure 10, the upper yield point occurs along the elastic line at a stress of 351.8 MPa. The modulus of elasticity was reported to be  $1.88 \times 10^5$  MPa measured between 131 MPa and 269 MPa [9]. Then there is a drop in stress to 328.2 MPa caused by the fracturing of the grain boundary walls by pent up dislocations, followed by a rapid multiplication of dislocations. This is followed by an extremely rapid drop in stress to the Breakthrough Stress at 211.1 MPa. This stress is well below the Lüders region and the lower yield point. The reason for this is that the specimen elongated much faster than the cross-head movement of the tensile testing machine, thereby relaxing the tension stress elastically. At the Breakthrough Stress the stress was not sufficiently large to cause dislocations to continue to move. Therefore, the stress was able to rise deforming the specimen elastically until plastic flow could continue. At that point deformation continued into the Lüders region to a strain of 0.010 which ended in the lower yield point at 294 MPa. After that, the stress rose and to a plateau of 317 MPa. This change in stress  $\Delta\sigma$  was 19.7 MPa. Plastic flow then continued at a constant value until a strain of 0.022 was reached. After that the stress increased with strain. The extensometer was removed at a strain of 0.0469 and a stress of 403.1 MPa. Deformation then continued until fracture at 328 MPa. The difference between the upper and lower yield points was 57.8 MPa for Specimen A, Figure 10. The average upper yield point of the three tests was 368.9 MPa. The average of the lower yield point of the three tests was 296.7 MPa. The average difference between the upper and lower yield points of the three tests was 77.3 MPa.

### 5.2. Stress-strain curves for polycrystalline iron, 14 ppm carbon

For Specimen C, the modulus of elasticity was  $1.69 \times 10^5$  MPa for Polycrystal iron, 14 ppm C, Figure 11 The tensile stress-strain curve shows that there was a gradual change from elastic deformation to plastic deformation to a yield stress of 202.7 MPa at 0.2% offset. There was no yield point since the grain boundary walls are segmented instead of being continuous around each grain, see Figure 8. Here the grain size was  $127\ \mu\text{m}$ . For plastic deformation to occur, dislocations pass between the cementite wall segments and through the disordered atoms at the grain boundaries. The stress to do this is very small resulting in a smooth transition from elastic to plastic flow with rising stress. As with steel, there were ripples in the "Ripple Stress Region". At its end, the stress jumped  $\Delta\sigma = 34.7$  MPa. Plastic flow then continued to rise smoothly to a strain of 0.0698.

### 5.3. Stress-strain curves for polycrystalline iron, 10 ppm carbon

Compression and tensile tests were performed on Polycrystal iron 10 ppm C at various temperatures from 293 K to 2.19 K, Altshuler [5]. The specimens had about 10 ppm carbon that was interstitial. The grain size diameter averaged  $28.4\ \mu\text{m}$ . The elastic constant was  $1.959 \times 10^5$  MPa at 293 K and  $2.059 \times 10^5$  MPa at 4.2 K, (figure C4[5]). The compression testing was done using a semi-automatic compression testing machine capable of testing 21 specimens sequentially at various cryogenic temperatures, Altshuler [5]. That decreased the time required for each test by a considerable amount. The specimens were cylindrical with a diameter of 0.050 inches (0.127 cm.) and a length of 0.100 inches (0.254 cm.). There was twinning as well as plastic deformation in tension

tests at 77 K and 20.4 K, (figure C3[5]). Compression testing suppressed fracture compared to tensile testing.

Figure 12 shows deformation in compression for polycrystalline iron, 10 ppm. There was plastic deformation prior to the upper yield point followed by a gradual drop in stress to the lower yield point. The difference between the upper and lower yield points at 293 K was 17 MPa, Altshuler (figure C69 [5]). Compared to that of the Polycrystal iron, 14 ppm C with a grain size of 127  $\mu\text{m}$ , the iron with the smaller grain size, 28.4  $\mu\text{m}$ , had 22% fewer dislocations piled up at the grain boundaries than that with the larger grain size. This results in a stress 230 MPa required for the start of yielding for the iron with a smaller grain size compared to 197 MPa for iron with the larger grain size. Yet, the flow stress was about the same at 250 MPa between 7% and 8% strain for both irons. Therefore, yield points, which have round tops, are seen with iron having smaller grain sizes. This type of yielding was also observed by NIST, see (figure 9[25] for pure iron containing 14 ppm carbon. SiGao (figure 2 [26]), showed plastic deformation from the elastic line for pure iron containing 20 ppm carbon. The average lower yield strength was  $\sigma_{ly} = 215$  MPa for the four national laboratories (figure 25 [25]). This was close to the lower yield point  $\sigma_{ly} = 204$  MPa for the Polycrystal iron, 10 ppm C, Altshuler (figure C69 [5]). These steels are saturated with interstitial carbon atoms. For these irons, the disordered atoms at the grain boundaries and differences in dislocation slip directions between adjoining grains are the governing mechanisms for deformation. This accounts for the stress difference between the upper and lower yield points of about 17 MPa compared to fracturing the grain boundary walls where the stress difference between the upper and lower yield point was about 77 MPa.

A universal method of comparing yielding between 293 K and 2.19 K was the extrapolated yield stress [5], see Figure 12. The reasons for this were:

- Below 90 K the difference between upper and lower yield stress disappears.
- Twinning occurred after slight plastic deformation.
- Very gradual transition between elastic and plastic deformation.

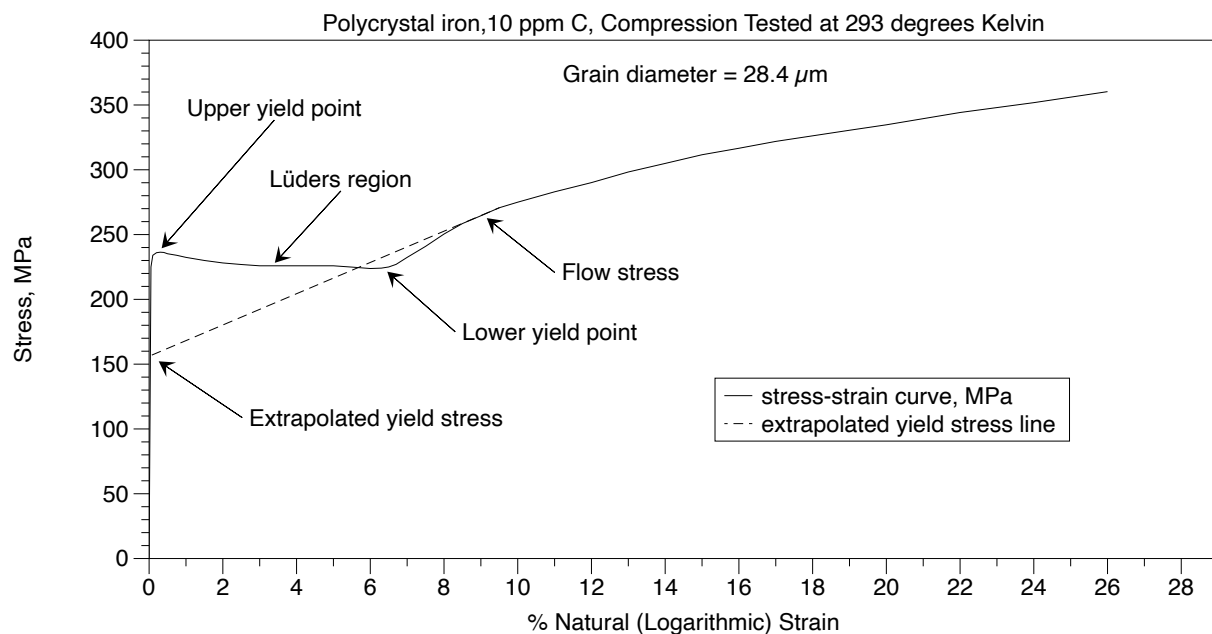


**Figure 12.** Polycrystal iron 10 ppm C, compression tested at 293 K.

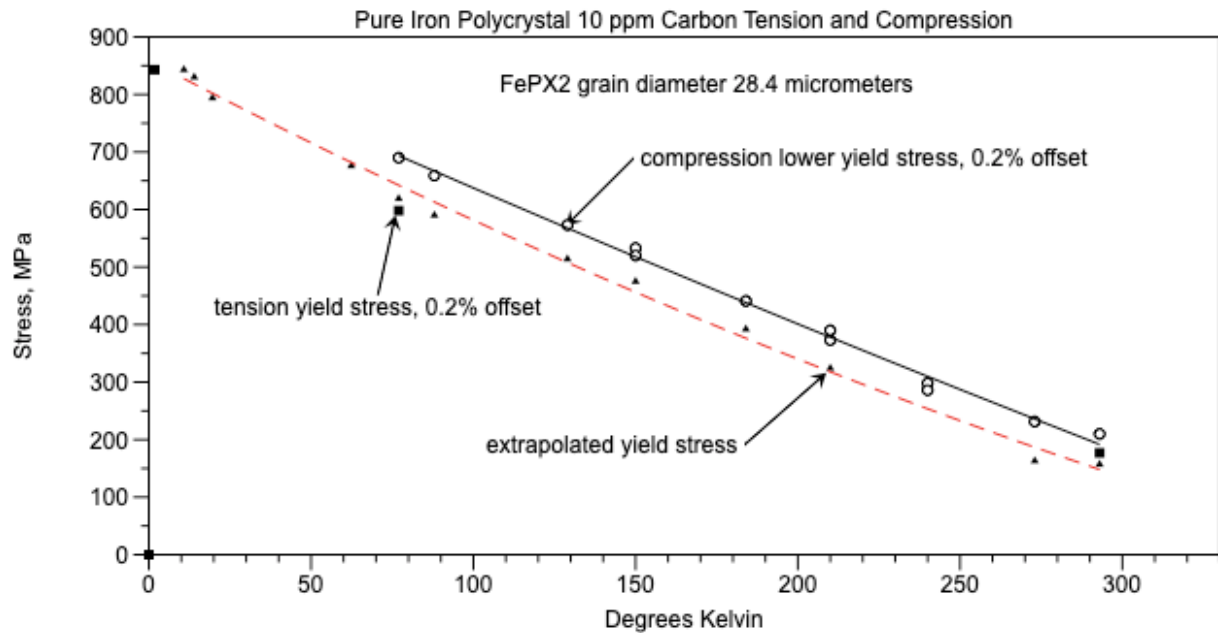


**Figure 13.** Pure polycrystal 10 ppm Carbon stress versus temperature.

The extrapolated yield stress versus temperature is shown in Figure 13, see the red dashed curve. This is the same as the tension yield stress at 0.2% offset. The stress rose as the temperature dropped from room temperature to 10 K. After that, the stress remained constant to 2.19 K, which is a real phenomenon with a probability of 95%, Altshuler and Christian [5,8]. The extrapolated lower yield stress ( $\sigma_y$ ) is given by equation (3).

$$\sigma_y = 859.1885038 - 2.958190766T + 0.0018123188392T^2 \quad (3)$$

#### 5.4. Single Crystal Iron 0.005 ppm C and 44 ppm C

Compression tests were performed on single crystals of high purity iron provided by Stein [7]. The iron crystals initially had 40 ppm carbon. They were purified by Stein using a  $ZrH_2$  treatment to a purity of 0.005 ppm C. Tests were performed in a manner like those described for Polycrystal Iron FePX2, Altshuler [5]. The compression axis was  $\bar{149}$ . The elastic constant was  $1.740 \times 10^5$  MPa at 293K and  $1.837 \times 10^5$  MPa at 4.2K, Altshuler (figure C4[5]) along the compression axis.

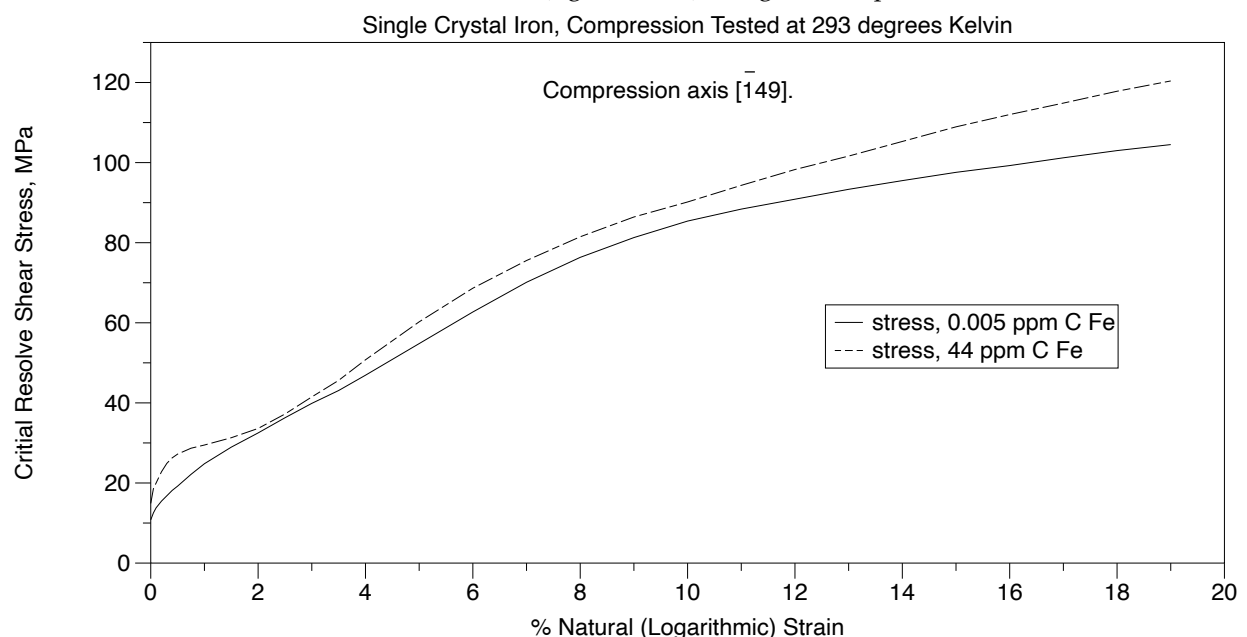


**Figure 14.** Single crystal iron, 0.005 ppm C and 44 ppm C, compression test at 293°K.

Figure 14 shows a comparison of the single crystal iron 0.005 ppm C to the single crystal iron 44 ppm C at 293 K, Altshuler (figure C28[5]). These tests eliminate the effect of grain boundaries and can therefore show the effect of solute carbon atoms on the critical resolved shear stress. Both crystals have the same other impurity elements. It is estimated that the 0.005 ppm carbon crystals could pin dislocations at every 281 unit cells, which is insufficient to significantly pin dislocations in terms of stress. Pure iron has 0.5 ppm carbon in solid solution at 0°C, Hume-Rothery [15]. Therefore the 44-ppm carbon single crystal would have sufficient carbon atoms that could pin dislocations every 22-unit cells. The critical resolved shear stress at 0.2% yield offset for the 0.005 ppm carbon single crystal iron was 15.47 MPa, and the 44-ppm single crystal iron was 22.8 MPa. The critical resolved shear stress at 0.05% yield offset for the 0.005 ppm carbon single crystal iron was 12.54 MPa, and the 44 ppm single crystal iron was 18.6 MPa with a difference of 6.1 MPa. For the 0.2% yield offset the difference between the 44 ppm C and 0.005 ppm C single crystals was 7.3 MPa at 293 K. At 77 K the difference was -12.7 MPa, Altshuler (figure C29[5]). These differences are very small compared to the difference between the upper and lower yield points of AISI 1018 steel which was 77.3 MPa.

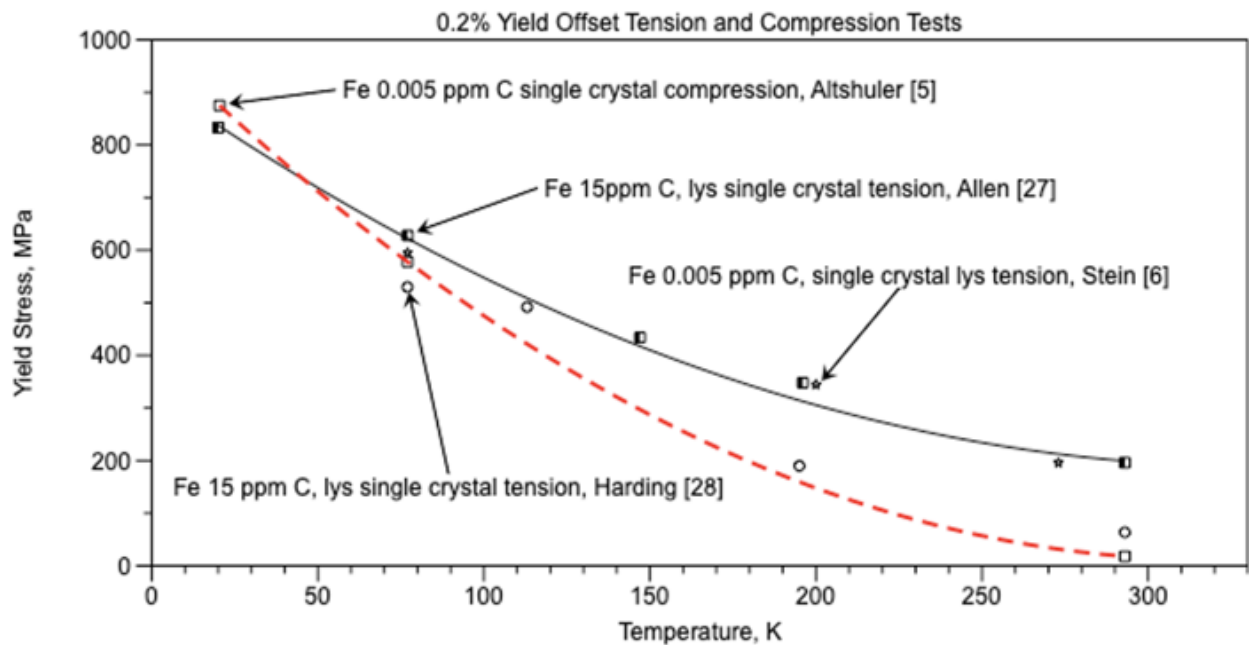


**Figure 15.** 0.2% Yield offset single crystal iron, tension, and compression tests.

Figure 15 presents single crystal tension tests by Stein [7] with 0.005 ppm C, Allen [27] with 27 ppm C, and Harding [28]. The tests by Altshuler [5] were done in compression while the other tests were done in tension. Here ( $\sigma_o$ ) is the 0.2% yield stress and T is absolute temperature for the single crystal iron, equation (4), the red dashed curve. The experimental results for this curve are considered the most reliable since the preparation of the specimens and tests were performed by author, Altshuler [5]. Specimen preparation is extremely important to ensure that they do not have significant work hardening that affects the yield stress as proven by Altshuler (figures C28[5] and C30[5]). These results agree with Harding [28]. Lower values of the yield stress are considered to be closest to the frictional stress of dislocations, see Figure 14.

$$\sigma_o = 997.343 - 6.19589T + 0.00973865T \quad (4)$$

### 5.5. Cottrell atmospheres pinning of dislocations

From the discussion of yielding of both pure single crystal iron with 0.005 ppm carbon and single crystal iron with 44 ppm carbon, section 5.4, pinning of dislocations by the Cottrell atmosphere, Cottrell [29], was not observed. Takeda [30] states that solid solution strengthening by nitrogen and

carbon would have a negligibly small influence on the yield strength of ferritic iron. **For steel that has cementite grain boundary walls that surround completely all the grain, the Cottrell atmosphere pinning of solute atoms is not the dominant cause for yielding.**

**These arguments support the hypothesis :**

*“The sharp upper yield point at the elastic line, followed by a rapid drop in stress to the lower yield point for ferritic hypoeutectoid steels, is caused by dislocations fracturing transversely cementite grain boundary walls that surround completely each grain.”*

## 6. Discussion and calculations about fracturing of iron and steel

The determination of the ductile brittle transition temperature is dependent upon the carbon content of the iron and steel. When there is sufficient carbon to form grain boundary walls that surround completely all of the grains, then cracks within the grains can propagate from grain to grain within the cementite grain boundary walls until fracture occurs. This is the condition that exist with steel. In the case of iron, where there is insufficient carbon to form grain boundary walls that surround completely each grain, cracks must propagate through ferrite grains to cause fracture. This requires considerably more stress than fracture propagation through cementite. Therefore, for the stress to reach a high enough level for brittle fracture in iron, the temperature must drop low enough for the onset of plastic deformation to rise to the brittle fracture stress, see Figure 13. The following discussion will show the difference in the ductile brittle transition temperature of steel and iron, see sections 6.3 and 6.4.

### 6.1. Equations for the Ductile Brittle Transition (DBT) of iron and steel

Cracks in the brittle grain boundary walls, Figure 7, are responsible for creating the brittle behavior of hypoeutectoid ferritic steels and pure iron at temperatures above twinning. It will be shown in the following discussion that predictions based upon propagation of these cracks can be made to determine correctly the ductile-brittle transition temperature ( $T_c$ ) for these metals.

The transition from ductile deformation to brittle fracture of iron and steel uses a combination of the Hall-Petch [31] equation (5) and the Griffith [1] equation (6).

Hall-Petch equation:

$$\sigma_y = \sigma_0 + k_y / \sqrt{D} \quad (5)$$

Where  $\sigma_y$  = lower yield stress

$\sigma_0$  = frictional stress

$k_y$  = material constant (Hall-Petch coefficient)

$D$  = average grain diameter

In equation (6), ( $\sigma_c$ ) is the critical fracture stress, ( $E$ ) is the elastic constant, ( $\gamma_s$ ) is the surface energy for the brittle crack/unit area, ( $c$ ) is the internal crack half length.

$$\sigma_c = (2E \gamma_s / \pi c)^{1/2} \quad (6)$$

For metals, Irwin [32] and Orowan [33] added a term for plastic deformation of crack tip which is considerable. Here, ( $\gamma_s$ ) is the surface energy of the sharp crack end and ( $\gamma_p$ ) is due to the plastic deformation required for propagation of the crack resulting in a blunted end, Tanaka (figure 5[34]).

$$\sigma_c = (2E (\gamma_s + \gamma_p) / \pi c)^{1/2} \quad (7)$$

$$\text{Critical stress intensity factor} = \text{fracture toughness: } k_{ic} = Y \sigma_c (\pi c)^{1/2} \quad (8)$$

Where  $Y$  is a geometry factor. For a crack inside an infinite body  $Y = 1.0$

Toughness defined:

$$G_c = k_{ic}^2 / E \quad (9)$$

Combining equations (7), (8) and (9), for  $Y = 1.0$

$$G_c = 2(\gamma_s + \gamma_p) \quad (10)$$

The length ( $L$ ) of an internal crack is equation (11) by combining equations (7) and (10).

$$L = 2c = 2EG_c / \pi \sigma_c^2 \quad (11)$$

The length ( $L$ ) of an internal crack is equation (12) by combining equations (10) and (11).

$$L = 4E(\gamma_s + \gamma_p) / \pi \sigma_c^2 \quad (12)$$

## 6.2. Relationship of the ductile-brittle transition temperature and stress with grain size.

### *Cementite grain boundary walls that surround all of the grains in steels*

A crack that is in a wall at one edge of a grain must grow longitudinally within the cementite wall extending along adjoining grains until the crack is sufficiently long to propagate through ferrite. Three factors govern the externally applied stress needed for a crack within a cementite boundary wall to propagate. These are:

1. Thermally activated stress to move dislocations in order to provide stress at the grain boundary.

Let  $\sigma_0$  = thermally activated stress. For iron and steel, this is the Peierls-Nabarro force, which causes a large increase in stress as temperature decreases, see Figure 15 and equation (4). The single crystal was used not having carbon, cracks or grain boundary interactions. Proof of the Peierls-Nabarro force in body centered cubic materials was given by Altshuler [5] and Altshuler and Christian [8].

2. Stress perpendicular to a crack thereby opening the crack in order that it propagates.

Let  $\sigma_p = \sigma$  be the stress perpendicular to the crack. This stress is given in equation (7).

3. Difference in the angle between the grain boundaries of two adjoining grains.

Let  $\theta$  = the angle between the grain boundaries of two adjoining grains. If the cementite grain boundary walls enclose all of the grains, then  $\theta$  is the angular change in direction as the wall lies at the grain boundary of one grain and its adjoining grain. Let  $\sigma_n$  = the stress at the crack that is in the direction of the externally applied stress. Then,

$$\sigma_p = \sigma_n (1 + \cos 2\theta)/2 \quad (13)$$

By combining these three factors, namely data from Figure 15 and equations (7) and (14), the externally applied stress  $\sigma_{ex}$  along the tensile axis is given in equation (14).

$$\sigma_{ex} = \sigma_0 + [8E(\gamma_s + \gamma_p) / 2\pi c]^{1/2} / (1 + \cos 2\theta) \quad (14)$$

For  $\theta = \pm 30^\circ$  the stress for continued crack growth increases by 33%. If  $\theta = \pm 60^\circ$  the stress increases by 400%, see Figure 5. Let  $\sigma_{ccem}$  be the stress for a crack to continue to propagate through cementite. Let  $\sigma_{cFe}$  = the stress for the crack to fracture through ferrite. The stress must then increase for continued propagation of the crack by  $(\sigma_{cFe} / \sigma_{ccem}) = [(\gamma_s + \gamma_p)/\gamma_s = 10.4/2.05 = 507\%]$ . This means that a crack must proceed along the cementite walls of adjoining grains until the stress increases to 507% of the stress required for the crack to propagate through a ferrite grain. Here the crack length is greater than the grain boundary edge  $L_0$ .

### *Cementite wall segments in iron*

Here a crack must stop at the ends of the segment until the stress increases to the point where it will proceed through ferrite. The length of the cementite grain boundary wall segment is affected by the grain size and carbon content. For larger grains, the segments are smaller than the grain edge. By rearranging equation (11) the result is shown in equation (15) and where the crack length  $L = 2c$  extends to the ends of the segment which is smaller than the grain edge  $L_0$ .

$$G_c = \pi L \sigma_c^2 / 2E \quad (15)$$

According to Pacyna and Mazur [35], toughness passes through a minimum at a certain grain size  $D_{min}$ . This can be seen in Reiser and Hartmaier (figure 6b [36]). Here the segments need to be larger than the grain edge length  $L_0$  for the toughness to increase. For the segment size to exceed the grain edge length, the crack size  $L$  becomes greater than the grain boundary edge and can extend along the edges of several adjoining grains. When the crack length equals the segment size the carbon content in the iron is shown in equation (16).

$$C_{min} = \xi_1 t / D \quad (16)$$

Where:  $C_0$  = total carbon content of iron

$C_{min}$  = carbon content of iron where the segment size equals  $L_0$

$\xi_1$  = constant estimated to be around  $1/6^{th}$  of  $C_{ow}$

$\xi_2$  = factor related to grain size  $D$  relative to  $D_{min}$

If the carbon content in the steel  $C_0$  is greater than  $C_{min}$ , then the length of the grain boundary segment will exceed the edge length of one grain according to equation (17).

$$L = L_0 \xi_2 C_0 / C_{\min} \quad (17)$$

A rough approximation would be that  $\xi_2 = 1.0$

Calculations for determining the externally applied stress for crack propagation can be found using equation (17). For cementite grain boundary segments that are smaller than the grain boundary edge  $L_0$ , the angle  $\theta = 0$ . Therefore the change in the external stress decreases slightly with decreasing grain size. This agrees with the findings of Werner et. al [37] where  $\alpha$ Fe fracture toughness is not affected by grain size. Werner states that this does not apply to  $\alpha$ -brass, since brass has no cementite walls and cracks form for other reasons. When the grain boundary segments exceed the grain boundary edge  $L_0$ , as is the case when the grain diameter  $D$  is smaller than  $D_{\min}$ , then there is a large increase in stress for propagation due to a large  $\theta$  for the crack to continue propagating. This behavior can be seen in Reiser and Hartmaier (figure 6b[36]).

### 6.3. Determination of the Hall-Petch constants

For hypoeutectoid ferritic steels and irons, the Hall-Petch equation **frictional stress**  $\sigma_0$  is shown in Figure 15 as  $(\sigma_y)$  and equation (6) from the data by Altshuler [5], the red dashed curve. The Hall-Petch **material constant**  $k_y$  results in equation (18) and Figure 16.

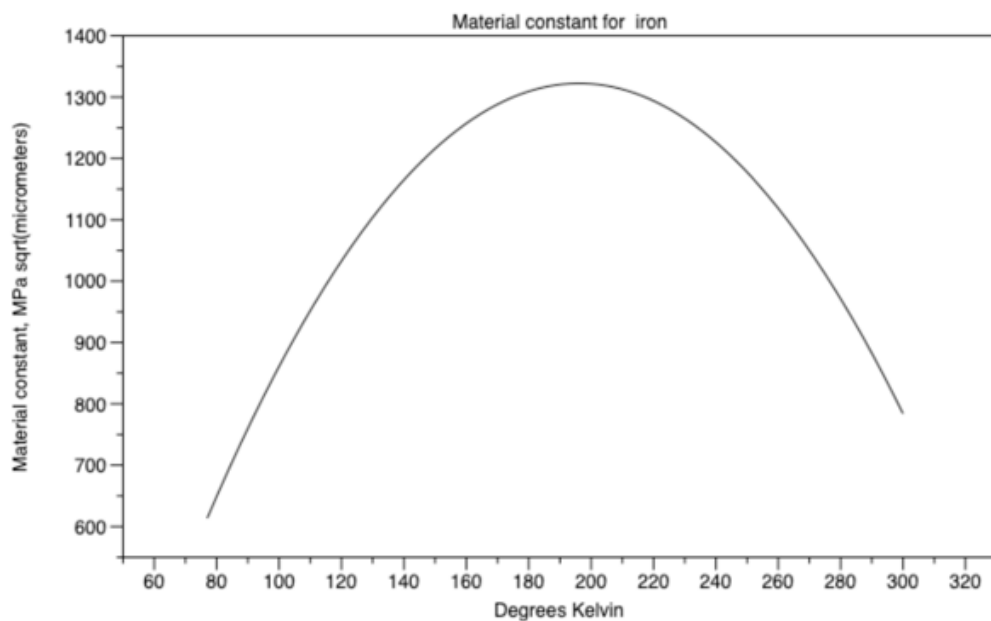


**Figure 16.** Material constant  $k_y$  for iron.

$$k_y = (\sigma_y - \sigma_0) \sqrt{D} = -736.25 + 17.254T - 0.042241T^2 \quad (18)$$

Since cracks in grain boundary walls can be used to correctly predict the temperature and stress at the ductile-brittle transition, the hypothesis “Cracks in the grain boundary walls are primarily responsible for the brittle behavior of iron and steel at and below the ductile-brittle transition temperature.” appears to have validity.

### 6.4. Determine fracturing of Polycrystal AISI 1018 Steel, 1900 ppm C

*Cementite grain boundary walls completely surround all of the grains.*

Determine the surface energies of cracks:  $\gamma_{\text{cem}}$ ,  $\gamma_s$ , and  $\gamma_p$ .

For AISI 1018 steel, the grains are surrounded by brittle grain boundary walls that have longitudinal cracks. With sufficient stress, it is reasonable that these cracks would grow within the walls longitudinally from grain to grain until the cracks are sufficiently large that they could fracture the ferrite grains transversely. Let  $\gamma_{\text{cem}}$  be the surface energy for a crack to propagate in the cementite grain boundary wall. According to Chiou and Carter (Table 6 [38]),  $\gamma_{\text{cem}} = 2.05 \text{ J/m}^2$  which is at (001)

the most stable fracture plane. Pure ferrite, has both brittle and plastic deformation at the crack tip. Schönecker et al. (figure 1[39]) theoretically determined  $\gamma_s = 2.527 \text{ J/m}^2$  at 0K and  $\gamma_s = 2.457 \text{ J/m}^2$  at 250K. Suzudo et al. (Table 1[40]), states that cleavage occurs along the {100} plane with  $\gamma_s = 2.542 \text{ J/m}^2$ . According to Chao (figure 4[37]),  $G_c = 20.4 \text{ J/m}^2$  for AISI 1018 steel. From equation (10)  $(\gamma_s + \gamma_p) = 10.2 \text{ J/m}^2$  and  $\gamma_p = 7.7 \text{ J/m}^2 = 7.7 \text{ MPa } \mu\text{m}$ .

#### Determine the Ductile - Brittle Transition

The ductile-brittle transition temperature (DBTT) for AISI 1018 steel was 5°C according to Chao et al. [41]. From Altshuler [2], the lower yield point of Polycrystal AISI 1018 steel  $\sigma_y = 294 \text{ MPa}$  at 23°C which extrapolates to 290 MPa at 5°C using yield point versus temperature data from Badaruddin et al [42]. Here the cementite grain boundary walls surround completely all of the grains in this steel. Cracks in these walls can propagate longitudinally with  $\gamma_{\text{cem}} = 2.05 \text{ J/m}^2$  from grain to grain. For a stress of 290 MPa and  $E = 212.66 \text{ GPa}$ , Koo [43] for the cementite {100} plane, the crack length needed for propagation in the wall would be  $L = 6.6 \text{ } \mu\text{m}$ , equation (12). Although this is larger than the average length of a wall edge of  $4.371 \text{ } \mu\text{m}$ , there could be grains with an edge of  $6.6 \text{ } \mu\text{m}$  or greater. As the stress increases to 290 MPa, the crack will grow longitudinally within the cementite wall until the stress required to propagate in the wall becomes greater than required for trans-granular fracture across the adjoining ferrite grain. To determine the crack length for fracture into ferrite, let  $E = 2.023 \times 10^5 \text{ MPa}$  for Polycrystal AISI 1018 steel. This is the average value for three tests made by Baxter [7]. Using  $G_c = 20.4 \text{ J/m}^2$ ,  $(\gamma_s + \gamma_p) = 10.2 \text{ J/m}^2$ , and  $\sigma_c = \sigma_y = 290 \text{ MPa}$  from equation (11), the internal crack length  $L = 31.2 \text{ } \mu\text{m}$  is required for the crack to propagate through a ferrite grain.

For DP590 steel, 0.08% C, the cementite grain boundaries probably were segmented. Therefore, a crack would propagate until it reaches the segment ends. Then the stress must rise until the stress is sufficient for the crack to continue to grow into ferrite. Assume the fracture stress  $\sigma_c$  was 400 MPa at -95°C similar to that shown for ferrite, Figure 13 and  $E = 200 \text{ GPa}$ . For  $G_c = 20.4 \text{ J/m}^2$  reported by Chao [40], then equation (11) yields a crack length  $L$  of  $16.2 \text{ } \mu\text{m}$ . That should be the segment length.

For low carbon steels, (0.15%C-0.3%Si-1.5%Mn), the cementite walls surround all the grains. From Inoui (equation 2[44]),

$$\sigma_c = 1.41 [ 2E (\gamma_s + \gamma_p) / \pi(1 - \nu) D ]^{1/2} \quad (19)$$

Using Poisson's ratio  $\nu = 0.291$ ,  $E = 2.10 \times 10^5 \text{ MPa}$ ,  $(\gamma_s + \gamma_p) = 10.2 \text{ J/m}^2$ ,  $D = 28.4 \text{ } \mu\text{m}$ , from equation (19)  $\sigma_c = 367 \text{ MPa}$ . The crack length  $L$  equals  $20.3 \text{ } \mu\text{m}$  from equation (12). The average length of an edge of a grain is about  $8 \text{ } \mu\text{m}$ . Therefore, the crack must propagate longitudinally along cementite grain boundary walls from grain to grain until the steel fractures transversely across ferrite grains.

#### *6.5. Determination of fracturing polycrystal pure iron, 10 ppm C*

##### *Segmented Grain Boundary Walls*

#### Determine the surface energy of cracks in Polycrystal iron, 10 ppm C

The fracture toughness of iron 99.999% purity is  $32 \text{ J/m}^2$  at 77K,  $68 \text{ J/m}^2$  at 173K, Hohenwater [45] for iron 90 ppm C, with a grain diameter  $D$  approximately  $5 \text{ } \mu\text{m}$ . From equation (2) and using  $t = 0.056 \text{ } \mu\text{m}$ , the carbon content would have to be 2,312 ppm for cementite walls to completely surround all of the grains. Therefore, the cementite walls are segmented. Extrapolating the fracture toughness to 20.4K,  $G_c = 21.2$  and  $(\gamma_s + \gamma_p) = 10.6 \text{ MPa } \mu\text{m}$ .

#### Determination of fracturing polycrystal pure iron, 10 ppm C *Segmented Grain Boundary Walls*

In pure iron the segmented cementite grain boundary walls probably have cracks for the same reason that AISI 1018 steel contains cracks in the walls, mainly due to thermal expansion differences between adjoining grains when the iron cools from austenitic temperatures to room temperature. From Altshuler (figure C3[5]), at  $T_c = 20.4\text{K}$ ,  $\sigma_c = \sigma_y = 750 \text{ MPa}$ . From equation (12) with  $E = 2.061 \times 10^5 \text{ MPa}$ , Altshuler (figure C4[5]), and  $(\gamma_s + \gamma_p) = 10.6 \text{ J/m}^2$ , the crack length ( $L$ ) was  $4.95 \text{ } \mu\text{m}$ . This length was smaller than the average edge length of a grain  $L_o = 7.8 \text{ } \mu\text{m}$  from equation (1) where  $D = 28.4 \text{ } \mu\text{m}$ . From Figure 13, equation (3),  $\sigma_c = \sigma_y = 799.6 \text{ MPa}$  and the crack length was  $4.35 \text{ } \mu\text{m}$ . Tension tests at 20.4K causes twinning and fracture of the test specimen. Compression tests on the other hand

suppress crack opening and is considered a true measure of initial dislocation motion. The reason for using equation (3) is the extrapolated yield stress is derived from the compression tests and has approximately the same value as the tension tests

**These arguments support the hypothesis :**

*“Cracks in the grain boundary walls are primarily responsible for the brittle behavior of iron and steel at temperatures below the ductile-brittle transition temperature.”*

#### 6.6. Fracture toughness and ductile-brittle transition temperature, published literature.

Tanaka [figure 3(a)[34]], shows that  $\alpha\text{Fe}$  has brittle failure at  $T_c = 101\text{K}$  for Fe-9%Cr (18 ppm carbon) tested at a strain rate of  $4.4 \times 10^{-4}$  with the activation enthalpy  $H = 0.21\text{ eV}$ . Since the activation enthalpy ( $H$ ) must be the same for both plastic and brittle failure,  $T_c$  can be determined.

From Altshuler and Christian (figure 20 [8]), for an activation enthalpy of 0.21 eV and a strain rate of  $5 \times 10^{-4}$  the temperature was 100K. These results agree with one another.

Hu et al [46] show that testing a X80 x D1422 mm Heavy-Wall Heat-Induced Seamless Bend pipe will cause a crack initiation and propagation that was trans-granular across the grains. The carbon content was 0.100%, and the grain size of three bend parts S1, S2, and S3 of the pipe were  $6.8\text{ }\mu\text{m}$ ,  $8.4\text{ }\mu\text{m}$  and  $13.7\text{ }\mu\text{m}$  respectively. Calculations using ( $C_{ow} = 0.207022\text{ t/D}$ ), and assuming a value of the cementite wall thickness of 62 nm, the carbon content of the walls for the grains would be 0.189% for S1, 0.153% for S2, and 0.094% for S3 of that which is needed to completely surround the grains. Therefore, it is concluded that grain boundary walls were segmented and fracture propagation would need to be trans-granular across ferrite grains. This is consistent with Hu (figure 12[46]). The greater the difference in the orientation between the grains, the greater the stress that is required for crack propagation (figure 9[39]).

Inoue et al (figure 14a [44]) gives the maximum tensile stress  $\sigma = 1674\text{ MPa}$  near the notch tip on the Charpy specimen for iron polycrystal, 0.15% C with an effective grain diameter  $D = 18\text{ }\mu\text{m}$ . The effective fracture stress  $\sigma_c = \sigma_y 560\text{ MPa}$ . This is between the extrapolated and compression yield stress in Figure 13.

## 7. Conclusions

### 7.1. Yielding of hypoeutectoid ferritic steels

- For annealed ferritic hypoeutectoid steels, the dominant factor that creates an upper yield point at the elastic line, followed by a sharp drop in stress to the lower yield point, is the existence of hard grain boundary walls enclosing the grains.
- Cementite ( $\text{Fe}_3\text{C}$ ) appears to form at the grain boundaries of polycrystalline ferritic hypoeutectoid steels and polycrystalline pure iron with as little as 14.4 ppm carbon.
- With sufficient carbon, these cementite grain boundary walls surround completely each grain, requiring that dislocations break across them for plastic deformation to take place. This is the primary cause for the upper yield point of ferritic hypoeutectoid steels.
- Due to the hardness of these cementite walls, a considerable amount of potential energy is pent up until the cementite walls between grain boundaries are broken. This allows dislocations to pass through the walls into the adjoining grains. As a result, there is a rapid drop in stress below the Lüders stress. This minimum stress is identified as the “Final Breakthrough Stress”.
- After the “Final Breakthrough Stress”, the stress first rises elastically and then plastically into the Lüders region and to the lower yield stress.

### 7.2. Yielding in pure iron

- Yielding in pure iron differ from that of steels since cementite grain boundary walls do not surround completely each grain.

- (b) Cementite grain boundary walls that do not surround completely each grain are due to insufficient carbon, but form segments of these walls instead. The segment length is governed by both grain diameter and carbon content.
- (c) Yielding occurs when dislocations break free of solute atoms, the Cottrell atmosphere, and pass around disordered atoms at the grain boundary, and then move in a different direction from one grain into the next one. This yielding is gradual from elastic deformation to plastic deformation.

### 7.3. Fracture in steel and iron

- (a) Cracks in cementite grain boundary walls are the primary cause of fracture of hypoeutectoid steels and iron.
- (b) The surface energy of a crack in cementite is  $2.05 \text{ J/m}^2$ , which propagates as a brittle type fracture. For propagation of a crack in ferrite where plastic deformation of the crack tip occurs, the surface energy of the crack is  $10.2 \text{ J/m}^2 = 10.2 \text{ MPa } \mu\text{m}$ .
- (c) If the cementite grain boundary walls surround completely the grains, a crack propagates longitudinally (**intergranular**) within these walls from grain to grain until the crack becomes sufficiently large to cause **trans-granular** fracture across the ferrite grains.
- (d) If the cementite grain boundary walls do not surround completely each grain and are segmented, then cracks grow to the segment ends and stop. The stress must then increase to cause trans-granular fracture across the ferrite grains.
- (e) When cementite walls are segmented:
  - For grains greater than a minimum diameter, the segment length is only governed by the grain diameter.
  - For grains smaller than a minimum diameter, the segment length is governed by both the grain diameter and carbon content.

## 8. Industrial Applications

New alloys could be developed as follows:

- **Atomic Force Microscopy could be used as a useful tool for developing new alloys.** For example, Atomic Force Microscopy of a metallographically prepared specimen of steel and iron can reveal the cementite grain boundary walls and whether they completely surround the grains or if they are segmented. This might save considerable time and expense in developing new alloys.
- Calculations can be made to determine the DBTT by using yield point versus temperature data found in Figure 13 and the Hall Petch parameters found in Figures 15 and 16. Therefore, new alloys of iron and steel could be developed without needing to perform a lot of expensive tests to be done at different temperatures.
- Composite materials might be made using fused 3 D deposition of metals in small prisms of varying shapes with alumina or diamond thin films. These films should be deposited to completely surround the prisms. A thin layer of an appropriate material might need to be deposited upon the diamond or alumina thin films to ensure proper bonding of the films to the prisms. The structure would be built up by alternating deposition of prisms and thin films. The final structure should be solid, perhaps after heat and pressure treatments. Here the prisms would be similar to grains of iron and the deposited films would be similar to cementite grain boundary walls. The resulting composite should have a much higher yield point than current

materials and yet be ductile after the upper yield point is reached. Rapid deposition methods would need to be developed to make such structures economically feasible.

**Author Contributions:** The author performed all the experimental work between 1990 and 1994 in his laboratory at the Advanced Materials Laboratory, Inc. The tensile tests and Atomic Force Microscopy performed between 2019 and 2022 were subcontracted by the author to other laboratories, see section 10, Funding. He wrote the manuscript as an independent researcher.

**Funding:** Thomas L. Altshuler paid commercial laboratories to perform specified experiments from his personal funds. He purchased the materials, designed the experiments specifying methods that were used, and interpreted the data. All other experimental work was done by him. He purchased ownership and the rights to publish the data obtained from the experiments. He obtained permission to publish the results of the data obtained. He subsequently wrote this manuscript.

**Data Availability Statement:** The raw and processed data required to reproduce these findings can be shared at this time and were downloaded on the web along with the manuscript by Altshuler [46]. Some of the actual materials used in the tests might also be available by contacting the author.

**Acknowledgements:** The author wishes to thank Professor Robert Rose for his very helpful suggestions that were used in the preparation of this manuscript. The author also wishes to thank Carolyn R. Currie for her suggestions in improving the clarity of this manuscript.

**Conflicts of Interest:** The authors declare that they have no known competing financial interests or personal relationships that could have appeared to influence the work reported in this paper.

## References

1. A. A. Griffith, "The Phenomena of Rupture and Flow of Solids", *Philosophical Transactions of the Royal Society of London*, (February 11, 1920), 163-198,
2. GoodFellow Corporation, 125 Hookstown Grade Road, Coraopolis, P 15108-9302. Pure iron purchased by Thomas L. Altshuler.
3. T. L. Altshuler, "Atomic-Scale Materials Characterization", *Advanced Materials and Processes*, vol. 130.3: , (1991), pp 18-23.
4. Thomas L. Altshuler, "Examination of Plain Carbon Steels Using an Atomic Force Microscope", *Atomic Force Microscopy/Scanning Tunneling Microscopy*, edited by Samuel H. Cohen, Springer Science + Business Media LLC, , (1994), pp 167-180.
5. T. L. Altshuler, "Deformation Processes in Body Centered Cubic Materials", *Doctor of Philosophy Thesis, Oxford University Department of Materials Science*, (1964).
6. Stein, D. F. 1963 Ph.D. Thesis, Rensselaer Polytechnic Institute, Troy NY.
7. D. F. Stein, J.R. Low and A. U. Seybolt, *Acta Metallurgica*. **11**, (1963), pp 1253
8. T. L. Altshuler and J.W. Christian, *Philosophical Transactions of the Royal Society of London*, Series A, Vol. 261, No. 1121 (Jun. 8, 1967), pp. 253-287
9. Thomas W. Baxter, Manager of Testing Services, Massachusetts Materials Research, Inc., 1500 Century Drive, West Boylston, MA 01583. MMR No. 131187 under contract with Thomas L. Altshuler, Project #111919.
10. Dr. Donald Chernoff, President Advanced Surface Microscopy, 3250 North Post Road, Suite 120 Indianapolis IN 46226, under contract with Thomas L. Altshuler.
11. T. Altshuler, "Yield Stress in Ferritic Steels Influenced by Grain Boundary Walls", *2021 AISTech Conference Proceedings*, PR-382-092, (June 29, 2021), pp. 955-948.
12. G.V. Shlyakhova, et. al., "Studying carbon steel by atomic force microscopy", (19 December 2018). *AIP Conference Proceedings* **2053**, 030063 (2018), Published Online; <https://doi.org/10.1063/1.5084424>
13. Martin Wells, personal communication, (February 1993).
14. C.J. McMahon, Jr., M. Cohen, "The fracture of polycrystalline iron", *Proceedings of the First International Conference on Fracture*, 2: (1965), 779-812.

15. Hume-Rothery, "Iron and its Interstitial Solid Solutions" (1966), *The Structure of Alloys of Iron*, Pergamon Press, Fig. 1.3, (May 5, 2006).
16. S. E. Offerman, "Grain Nucleation and Growth During Phase Transformations", (2002), <https://science.sciencemag.org/content/298/5595/1003>.
17. K. Lu et al. "Grain Boundary Plays a Key Role in Carbon Diffusion in Carbon Irons Revealed by a ReaxFF Study", *J. Phys. Chem. C*, **40**, (122), (2018), pp. 23191-23199,
18. K. D. N. Bhadeshia, "Interpretation of the Microstructure of Steels", (2008) [https://www.phase-trans.msm.cam.ac.uk/2008/Steel\\_Microstructure](https://www.phase-trans.msm.cam.ac.uk/2008/Steel_Microstructure)
19. A. Pandit, "Theory of Pearlite Transformation in Steels", Doctor of Philosophy Thesis, University of Cambridge Department of Materials Science and Metallurgy, (June 2011).
20. R. Song, D. Ponge, R. Kaspar, D. Raabe, (2004) [https://www.academia.edu/.../Grain\\_boundary\\_characterization\\_and\\_grain\\_size\\_measurement\\_in\\_an\\_ultrafine-grained\\_steel](https://www.academia.edu/.../Grain_boundary_characterization_and_grain_size_measurement_in_an_ultrafine-grained_steel)
21. J. Takahashi, "Quantitative Observation of Grain Boundary Carbon Segregation in Bake-Hardened Steels", *Nippon Steel Technical Report*, No. 91, (January 2005).
22. W. Bin, "Precipitation behavior of nanoscale cementite in hypoeutectoid steels during ultra-fast cooling (UFC) and their strengthening effects", *Materials Science and Engineering: A*, **575**, (15 July 2013), pp. 189-198.
23. T. Ogawa, et. al., "Evaluation of tensile properties of ferrite single-phase low carbon steel with different initial microstructures", *AIMS Materials Science*, 6(5): (September 2019), pp 798-805
24. A. Ganeev, et al "On the nature of high-strength state of carbon steel produced by severe plastic deformation", *IOP Conf. Series: Materials Science and Engineering* **63**, (2014), pp 01212.
25. Enrico Lucon, Kenji Abiko, Marlies Lambrecht, Birgit Rehmer, "Tensile Properties of Commercially Pure, High Purity, and Ultra-High Purity Iron: Results of an International Round Robin", *NIST Technical Note 1879*, (April 2015).
26. SiGao, MeichuanChen, ShuaiChen, NaoyaKamikawa, AkinobuShibata, and Nobuhiro Tsuji, "Yielding Behavior and Its Effect on Uniform Elongation of Fine Grained IF Steel", *Materials Transactions*, Vo. 55, No. 1, (2014), pp. 73 to 77.
27. N.P. Allen, B.E. Hopkins and J.E. McLennan, "The Tensile Properties of Single Crystals of High-Purity Iron at Temperatures from 100 to -253 degrees C", *Proceedings of the Royal Society of London. Series A, Mathematical and Physical Sciences* Vol. 234, No. 1197, (Feb. 7, (1956), pp. 221-246.
28. J. Harding, "The Yield and Fracture Behaviour of High-Purity Iron Single Crystals at High Rates Crystals at High Rates of Strain", *Proceedings of the Royal Society of London. Series A, Mathematical and Physical Sciences* Vol. 299, No. 1459, (July 25, 1967), pp. 464-490.
29. A.H. Cottrell, A. H.; Bilby, B. A., *Proceedings of the Physical Society*, **62** (1), (1949), pp 49-62, Bibcode: 1949PPSA...62...49C, doi: 10.1088/0370-1298/62/1/308.
30. T. Takeda, et al "Effect of Interstitial Elements on Hall-Petch Coefficient of Ferritic Iron", *ISIJ International*, **48**(8), (January 2008), pp. 1122-1125.
31. N. J. Petch, "The cleavage strength of polycrystals", *J. Iron and Steel Inst.*, vol.174, (1953), pp 25-28.
32. Irwin, G.R., "Fracture Dynamics, *Fracturing of Metals*", American Society for Metals, Cleveland, OH, (1948), pp. 147-166.
33. Orowan, E., "Fracture and Strength of Solids," *Reports on Progress in Physics*, Vol. XII, , (1948), pp. 185.
34. Tanaka, M., Wilkinson, A.J., Roberts, S.G., "Ductile-brittle transition of polycrystalline iron- chromium alloys", *Journal of Nuclear Materials*, 378, (2008), pp 305-311.
35. Pacyna J, Mazur A. The influence of grain size upon the fracture toughness of hot-work tool steel. *Scand. J. Met.*; **12**, (1983), pp 22-28.
36. Reiser J., Hartmaier, A., "Elucidating the dual role of grain boundaries as dislocation sources and obstacles as its impact on toughness and brittle-to-ductile transition", *Sci. Rep.* **10**, (2020), pp. 27939.
37. Werner E. Der Einfluß der Korngröße, des Legierungsgehaltes und einer Kaltumformung auf die Bruchzähigkeit. *Z. Metallkd.*, **79**, (1988), pp 585-590.
38. Chiou Jr., W.C., Carter, E.A., "Structure and stability of Fe<sub>3</sub>C cementite from first principles", (2002), pp 87-100 [www.sciencedirect.com](http://www.sciencedirect.com).
39. Scho"necker, Xiaoqing Li, Bo"rje S., Johansson, S.K., Kwon, "Thermal surface free energy and stress of iron", *Scientific Reports*, 5(1): (October 2015), pp 14860.
40. Suzudo T, Ebihara K, Tsuru T, and Mori H, "Cleavage along {110} in bcc iron emit dislocations from the curved crack fronts", *Scientific Reports* **12**, Article number: 1970, (2022).
41. Chao, Y.J., Ward Jr, J.D, and Sands, R.G., "Fracture Impact Energy and Ductile-Brittle Transition Temperature of Dual-Phase 590 Steel.", *SAE Transactions*, Vol. 114, Section 5: Journal of Materials and Manufacturing, (2005), pp. 708-712.
42. Badaruddin, M., Wardono Zulhanif, H., H. Supriadi, Salimor, M.,, "Experimental investigation of mechanical properties of cold-drawn AISI 1018 steel at high-temperature steady-state conditions", *Journal of Materials Research and Technology*, Vol. 8, Issue 2, (April 2020). pp 1893-1904.

43. Koo BW, Chang YJ, Hong S-P, Kang CS “Experimental Measurement of Young’s Modulus from a Single Crystalline Cementite”, *Scripta Materialia*, 82(S3) , (July 2014), pp. 25-28.
44. Inoue T, Qiu H., Ueji R., Kimura Y., “Ductile-to-Brittle Transition and Brittle Fracture Stress of Ultrafine-Grained Low Carbon Steel”, *Materials* 2021, **14**(7), (2021), p 1634.
45. Hohenwarter, A. and Pippan, R., “Fracture of ECAP-deformed iron and the role of extrinsic toughening mechanisms”, *Acta Mater*, 61(8), (May 2013), pp 2973-298. Acta doi: 10.1016/j.actamat.2013.01.057 Mater.
46. Hu J., Liu Y., Wang G., Li Q., “Effects of Microstructure on the Low-Temperature of an X80 x D1422 mm Heavy-Wall Heat-Induced Seamless Bend”, *Metals* 2021, **11**, (2021), pp. 1055.
47. Altshuler, Thomas, “Brittle Fracture of Iron and Steel and the Sharp Upper Yield Point are Caused by Cementite Grain Boundary Walls”, (August 23, 2023, updated 04/26/2024). Available at SSRN: <https://ssrn.com/abstract=4588927> or <http://dx.doi.org/10.2139/ssrn.4588927>

**Disclaimer/Publisher’s Note:** The statements, opinions and data contained in all publications are solely those of the individual author(s) and contributor(s) and not of MDPI and/or the editor(s). MDPI and/or the editor(s) disclaim responsibility for any injury to people or property resulting from any ideas, methods, instructions or products referred to in the content.